Computational Screening of Fly Ash Zeolite Sorbents for Boric Acid Removal

John Findley[a,b], Evan J. Granite[c], Eric Grol[a], and Janice A. Steckel*[,a]

[a] U.S. Department of Energy, National Energy Technology Laboratory, 626 Cochran's Mill Rd, Pittsburgh, PA 15236, United States

[b] NETL Support Contractor, U.S. Department of Energy, National Energy Technology Laboratory, 626 Cochran's Mill Rd, Pittsburgh, PA 15236, United States

[c] U.S. Department of Energy, 1000 Independence Ave., S.W., Washington, DC 20585, United States

*Corresponding author e-mail: steckel@netl.doe.gov

Abstract

In the U.S., many impoundments at coal-fired power plants contain elevated contaminants like arsenic, boron, barium, and selenium. Zeolites synthesized from fly ash show promise as sorbents for these contaminants. However, optimizing sorption capacity is challenging due to numerous possible topologies, silicon to aluminum (Si/Al) ratios, and cation types. In this study, molecular simulations are used to design cationic zeolites for boric acid adsorption. Force field models based on quantum mechanical calculations (PBE+D2) for Na-, Ca-, Mn-, and Fe-exchanged chabazite and LTA are presented. The new D2FF force fields reproduce DFT energies with about half the error of UFF. Zeolite performance depends on Si/Al ratio and cation type, with low Si/Al ratio chabazite (CHA) and phillipsite (PHI) zeolite frameworks exchanged with Ca2+ or Na+/Ca2+ mixtures showing the highest adsorption. These findings suggest tailored fly ash-derived zeolites could provide effective boron removal from leachate ponds.

Topical Heading

Thermodynamics and Molecular-Scale Phenomena

Keywords

Adsorption, Zeolite, Fly ash, Impoundment, Boron, Boric acid, Density Functional Theory, Monte Carlo, Force Field, Coal Combustion Residuals, Water, Sorbent, Screening

1. Introduction

Coal used in the United States to make electricity has resulted in approximately two billion tons of coal combustion byproducts stored within impoundments. Impoundment ponds are landfills intended to securely store coal combustion byproducts such as fly ash and bottom ash, and prevent the release of contaminants such as arsenic, boron, mercury, and selenium, into the environment.[1–5]. While boron can be beneficial in small amounts, high levels of boron can cause health issues such as nausea, headache, diarrhea, and kidney damage in humans and animals.[1,6] Excess boron can also be detrimental to crop growth and reproduction.[7] Boron levels are currently not regulated at the federal level in the United States, but some states have limits on boron concentration in water. The World Health Organization's guideline for boron concentration is 0.5 mg/L.[6] This is significantly lower than the typical concentration of boron in impoundment ponds based on reports by the Electric Power Research Institute (EPRI), which observed median boron concentrations on the order of 1 mg/L to 10 mg/L in impoundment water depending on the coal type and measurement method.[3] Typical methods for boron cleanup include chemical precipitation, ion exchange, liquid-liquid extraction, and adsorption.[1,8–10]

Adsorption is a promising cleanup method for capturing boron from aqueous solutions. In water, boron typically exists as boric acid (H_3BO_3) or borate ($[B(OH)_4]^-$) depending on the pH[11]. Studies have demonstrated adsorption on activated carbons[12], metal oxides[10], and cation-exchanged zeolites.[13,14] Zeolite sorbents can be made from waste coal fly ash, which contains silicon and aluminum oxides, using hydrothermal synthesis.[15–17].

Zeolites are a class of nanoporous aluminosilicate materials commonly used as commercial adsorbents and catalysts.[15–24] The International Zeolite Association (IZA) database recognizes almost 250 distinct zeolite topologies that have been synthesized experimentally.[25] Additionally, millions of hypothetical zeolite topologies have been predicted.[26,27] Zeolites have been widely used industrially for separations[28–31] in sorbents and membranes, and in catalysts.[32–35]

There is a realistic potential for waste fly ash to be used for making sorbents that can be used for boron removal. Nine zeolite topologies (ANA, CHA, FAU, GIS, LTA, LTF, LTL, PHI, and SOD) have been synthesized from coal fly ash.[15] These zeolites can be synthesized with various Si/Al ratios, and the identity of extra-framework cations can be tuned using ion exchange. Also, the topology of zeolites can be tuned using organic structure-directing agents during synthesis.[36–39] These synthetic methods render a large variety of zeolite structures synthetically accessible.

While boron uptake by various sorbents including surfactant modified zeolites, metal organic frameworks, activated carbon, fly ash or zeolites have been reported, comparison of these studies with simulation is limited by inexact characterization of the sorbents or studies based on mixtures.[8,40–43] With modified zeolites or other materials, a wide range of uptakes up to 10 mg/g from highly alkaline solutions containing a range of loadings were reported. However, issues have been reported with stability of both metal organic frameworks and surface modified zeolites, in contrast to zeolites which have been noted for their stability.[44–46] These works serve to highlight

interest in the development of effective sorbents for boron, but uptake was measured at impractical pH levels.[2] Yüksel et al. investigated boron removal from aqueous solution using fly ash, zeolite, and demineralized lignite.[13] Uptake was affected by the pH of solution with the maximum adsorption observed at pH 10, in which boron is in the form of borate. The zeolite used in the study was a mix of several minerals, complicating any comparison with simulations.[47] The authors reported a boron removal efficiency of 15.8% for sorbent loading of 50 g L^{-1} in a solution with initial boron concentration of 1 mmol L^{-1}. The uptake performance of fly ash exceeded that of the zeolite and demineralized lignite used in their study. Kluczka et al. reported absorption of boron from solution using a zeolite synthesized from fly ash.[48] The uptake, obtained at pH=7 from a solution with 50 mg B L^{-1}, was 2.3 mg g^{-1} with an adsorbent dose of 20 g L^{-1}. At pH=7 the predominant species in solution would be boric acid. In both reports of experiments, the materials studied were a mixture of minerals with zeolites. Additionally, the Si/Al ratio of the zeolite phase was not analyzed. Typically, clinoptilolite, like the zeolite studied by Yüksel et al, has a Si/Al ratio higher than 4.[49] However, the presence of charge balancing cations, associated with Al substitutions in the framework, have been associated with high adsorption of polar adsorbates [31,50,51], which indicates that a low Si/Al ratio zeolite would be more promising for boron removal, rather than a high Si/Al ratio zeolite. This, coupled with the variety of pore structures of zeolites that have been synthesized from fly ash[15] suggest that the performance of zeolites for boron removal can be enhanced by examining the combined effects of zeolite structure, Si/Al ratio, and extra-framework cation species.

Experimental screening of zeolites for a given application can be time-consuming and expensive due to the tunability of zeolite composition and a variety of experimental conditions. Therefore, it is common to use atomistic simulations for materials screening. First-principles quantum mechanical (QM) calculations have been used to accurately predict binding energies and geometries of adsorbates in nanoporous materials.[52–55] However, these methods are too slow to compute macroscopic properties such as heats of adsorption and adsorption isotherms because these computations can require averaging over millions of microstates to get a converged thermodynamic property. Using interatomic potential energies based on model potentials or force fields (FFs) speeds up energy calculations required for Grand Canonical Monte Carlo (GCMC) simulations and makes possible computation of equilibrium adsorption isotherms. While most force fields cannot describe chemical reactions involving bond formation and breaking, they can be used in statistical mechanics calculations to predict phase equilibrium, adsorption and diffusion of adsorbates in porous materials.[52,54,56–58] Force fields are often used for materials screening for adsorption applications.[59–62]

Force fields capable of modeling boric acid interacting with a range of cationic zeolites were limited to generic force fields such as UFF[63] and Dreiding[64,65]. While generic force fields have been used for initial screening studies[65–67], they can lack accuracy for certain zeolites. For instance, Findley and Sholl saw that generic force fields performed poorly for predictions of CO_2 uptake in $GaPO_4$ zeolites[67]. Pairwise classical force fields parameterized based on experimental data [68,69] or ab-initio calculations[54,57,67,70–74] have demonstrated reasonable transferability in porous

materials. Using a large set of experimental data for training, the TraPPE Zeo force field was able to fit a Lennard-Jones and coulomb potential to describe adsorption for a large set of adsorbates in pure-silica zeolites. Force fields fit to dispersion-corrected density functional theory calculations were able to accurately predict the uptake of a variety of hydrocarbons as well as CO_2, N_2, O_2, and H_2O by fitting to a Lennard-Jones and coulomb potential. Despite the simplicity of the functional form, these force field predictions gave reasonable adsorption and diffusion predictions across zeolite topology and Si/Al ratio, and extra-framework cation species (Li^+, Na^+, K^+, Rb^+, Cs^+). However, to our knowledge there are no existing force fields explicitly parametrized for predicting H_3BO_3 adsorption in cationic zeolites.

In this work, force field models were fit to dispersion-corrected density functional theory calculations following previously established methods[54,57,67,70–75] to predict the adsorption of boric acid and water in cationic zeolites. Boric acid is modeled because it has been shown that it is the most common species of boron for pH < 9 with >99% boric acid at a pH of 7[11]. Grand Canonical Monte Carlo simulations were performed to predict the adsorption of boric acid from 1-20 ppm aqueous solution for a set of zeolites with Si/Al ratios ranging from 1 to 9. The zeolites contained a combination of extra-framework Na^+, Ca^{2+}, Fe(II), and Mn(II). Na^+ was selected because Na-exchanged zeolites are widely available. Ca^{2+} was selected because of the higher charge per cation. Fe and Mn were selected because they have been shown previously to effectively remove similar contaminants (H_3AsO_3 and H_3AsO_4) from water[76]. Our results highlight how Si/Al ratio, cation identity, and zeolite framework structure influence boric acid adsorption from aqueous solution.

2. Materials and Methods

2.1 Zeolite Framework Models

For the computation of boric acid sorption, we selected zeolites that were previously synthesized using fly ash[15] or are well-studied zeolites. The coordinates for the tetrahedral atoms (Si or Al) and O atoms for each zeolite topology (CHA, DDR, FAU, FER, GIS, LTA, LTL, MEL, MFI, PHI, TON) were taken from the International Zeolite Association (IZA) database.[25] For all zeolites in this study, the frameworks were expanded such that all cell vectors had lengths of at least 20 Å. For each pure silica framework, aluminosilicate frameworks were created with Si/Al ratios of 1, 2, 3, 4 and 9 by substituting Al for randomly chosen Si atoms in the framework subject to Löwenstein's rule.[77] Although some of these zeolite topologies, such as FER[35,78] and CHA[34,79] can have nonrandom distributions of Al, the distribution of Al in most zeolites is unknown.[80] Therefore, a random Al distribution was used for all zeolites in the structure database. For each of the aluminosilicate zeolites, extra-framework cation positions were assigned using parallel tempering.[81]

2.2 Density Functional Theory Calculations

Periodic density functional theory (DFT) calculations based on the projector augmented wave (PAW) formalism were performed using the VASP code.[82–84] An energy cutoff of 520 eV was used for the plane-wave basis set to represent valence electrons (H:$1s^1$, B:$2s^2 2p^1$, O:$2s^2 2p^4$, Si:$3s^2 3p^2$, Al:$3s^2 3p^1$, Li:$1s^2 2s^1$, Na:$2p^6 3s^1$, K:$3p^6 4s^1$, Ca:$3p^6 4s^2$, Mn:$3p^6 3d^5 4s^2$, Fe:$3d^7 4s^1$). The zeolites in these calculations had large unit cells and thus only one k-point at the Γ-point of the Brillouin zone was necessary. The Perdew-Burke-Ernzerhof (PBE) exchange and correlation functional with the D2 dispersion correction from Grimme[85] was used for all DFT calculations. The PBE+D2 method was selected rather than the newer PBE+D3 method in order to maintain consistency with parameters fit by Fang et al.[57] A comparison of a sample of 1000 PBE+D2 and PBE+D3 calculations showed agreement in adsorption energetics to within 3% as shown in the Supporting Information **Figure S1**. The density-derived electrostatic and chemical method (DDEC3) was used to assign atomic point charges based on electronic densities from DFT calculations.[86,87] Spin-polarized calculations were used to model zeolites containing Mn or Fe and the magnetic ordering was assumed to be ferromagnetic. Ab initio molecular dynamics (AIMD) calculations were performed at 300 K with a 0.1 fs timestep.

2.3 Cation-Zeolite Force Field

The force fields for cation-framework interactions were fit to reproduce the energies of PBE+D2 calculations following the procedure of Fang et al.[57,88] The validity of the force fields derived in this work was demonstrated by the fact that they accurately predict the distributions of extra-framework Na and K in zeolites. The parameters of Na-Oz were taken directly from work by Fang et al.[57] This work used a Buckingham + Coulomb potential to describe cation-framework interactions (E_{FF})

$$E_{FF}(R_{ij}) = A_{ij} e^{-B_{ij} R_{ij}} - \frac{C_{ij}}{R_{ij}^6} + \frac{q_i q_j}{R_{ij}} \quad (1)$$

where R_{ij} is the distance between atom i and atom j. A_{ij}, B_{ij}, and C_{ij} are fitted Buckingham potential parameters, and q_i and q_j are the point charges on atom i and atom j. To maintain consistency with the work of Fang et al.[57] across all species of extra-framework cations, the DDEC3 method was used to assign point charges for the remaining cations (Ca, Mn, Fe).

LTA zeolites with Si/Al = 3 were used for fitting cation-framework interactions due to the high symmetry of LTA, as well as the small unit cell size (< 80 atoms). When fitting cation-framework interactions for Ca^{2+}, Mn(II), and Fe(II), the experimental atomic coordinates for framework (Si, Al, O) atoms in Ca-LTA from Pluth and Smith[89] were used. Initially, three extra-framework cations were placed in the centers of three different 6-membered rings, which has been shown experimentally to be the most favorable location for divalent cations.[89] Starting from these initial configurations, the positions of extra-framework cations were relaxed using DFT, while holding the positions of framework (Si, Al, O) atoms fixed. When generating a training set for cation-framework interactions, each distinct cation position was selected and 500 random

translation moves were performed with a maximum displacement of 1 Å from the site while holding all other cations fixed in their equilibrium positions, as in Boulfelfel et al.[90] . The energy of each configuration was then computed using PBE+D2.

To avoid performing calculations in frameworks with net charges during the fitting process, the force field was fit to reproduce relative PBE+D2 energies, using the initial framework and equilibrium positions as the reference state. Coulomb energies were also computed relative to the reference configuration using DDEC3 point charges for framework atoms and extra-framework cations. The Coulomb energies were then subtracted from the relative PBE+D2 energies to give relative van der Waals (vdW) energies, which were used to fit the parameters of the Buckingham potential. Parity plots showing a comparison between force field and DFT energies are shown in **Figures S2-S4** of the Supporting Information. Force field parameters for cation-framework interactions are shown in **Table S1**. A comparison of predicted cation distributions with experimental data is shown in Section 3.1 as well as in **Tables S2** and **S3** of the Supporting Information.

2.4 Adsorbate-Zeolite Force Field Models

Available force fields for boric acid interacting with a wide range of cationic zeolites were limited to generic force fields such as UFF[63] and Drieding[64]. Therefore, PBE+D2-derived force fields (D2FFs) for adsorbate-zeolite interactions were fit using a cyclical procedure similar to the methodology in Findley et al.[67], in which force fields were fit to predict CO_2 and H_2O adsorption in $AlPO_4$ and $GaPO_4$ zeolites. Dispersion-corrected density functional theory based force fields have shown success in predicting experimental adsorption isotherms in porous materials without relying on experimental data as an input.[54,88] Force fields derived based on various ab-initio methods using this cyclical method have been developed for gas adsorption and diffusion in zeolites and metal-organic frameworks (MOFs),[54,57,67,70–74]

First, an initial set of 1000 configurations for a single adsorbate molecule (H_2O or H_3BO_3) in a zeolite with (CHA, Si/Al = 3.5 for H_3BO_3 and LTA, Si/Al = 3 for H_2O) were generated using NVT Monte Carlo in RASPA[91] at 300 K with 10^5 trial moves. The relatively small unit cell of CHA allowed for effective sampling of the repulsive region of the Lennard-Jones potential as well as the interactions of H_3BO_3 with multiple cations at once. (See **Figure 1**.) The initial adsorbate-zeolite parameters came from applying Lorentz-Berthelot mixing rules between adsorbate models and adsorbent atoms. The Dreiding force field[64] was used for initial Lennard-Jones parameters for adsorbent atoms and extra-framework cations.

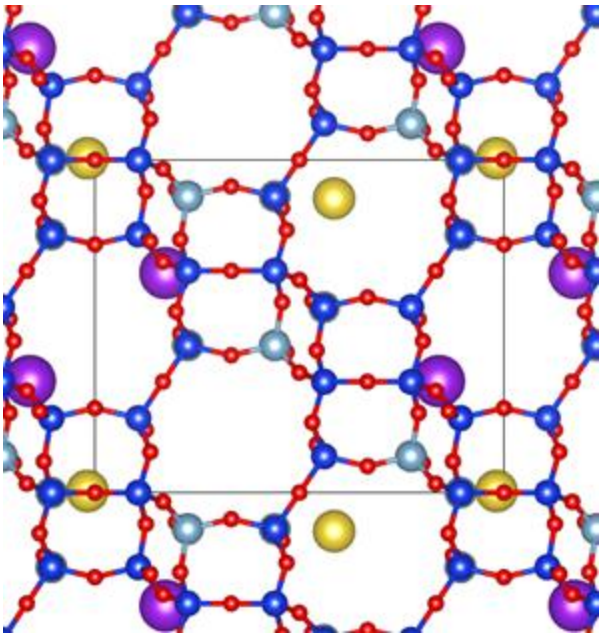

Figure 1: The unit cell of Ca-CHA (Si/Al = 3.5) used to train force field parameters for boric acid - Ca interactions is shown. The image includes atoms outside the periodic boundaries to more clearly present the 8-membered rings present in this structure. To ensure a robust sample of H_3BO_3-Ca distances, two Ca ions were placed in 8-membered rings (yellow), while the remaining two Ca ions were placed in 6-membered rings (purple).

The energy for each configuration in the training set was computed using DFT. Interaction energies were computed by taking the single point energy of the adsorbate+adsorbent and subtracting the values of the empty adsorbent and isolated adsorbate. Coulombic energies were calculated using the Ewald summation method. Next, vdW energies were obtained for each configuration by subtracting the Coulomb energies from the DFT energies. These energies were fit to either a Lennard-Jones potential or a Buckingham potential if the Lennard-Jones potential could not provide a good fit. Parity plots comparing DFT and force field adsorbate-zeolite interaction energies are shown for the final iteration of force field fitting in **Figures S5-S13** of the Supporting Information. Root mean squared errors (RMSEs) for boric acid-zeolite interactions ranged from 3.45 kJ/mol to 10.3 kJ/mol. RMSEs for water-zeolite interactions ranged from 2.42 kJ/mol to 6.41 kJ/mol. These values are comparable to the force field fitting errors observed for C_2H_6 - zeolite (4.3 kJ/mol) and C_3H_8 - zeolite (4.8 kJ/mol) interactions in Fang et al.[75]; their fitted parameters were subsequently used to accurately predict adsorption isotherms. A justification for why the Buckingham potential outperformed the Lennard-Jones potential for Ca-H_2O interactions is shown in **Figure S14** of the Supporting Information. To reduce potential bias from the initial force field, the newly-fit force field was used to generate a new set of 1000 configurations and the same procedure was repeated until force field parameters converged to within 10% between previous and subsequent iterations. The fitted D2FF force field parameters are shown in **Table S4**.

2.5 Adsorbate Models

For calculations involving water, the SPC/E model was used because of the model's compatibility with validated zeolite oxygen forcefield parameters.[80] The boric acid model geometry was taken from the work of Otkidach and Pletnev and was also used to describe boric acid - boric acid interactions.[92] However, a new model was fit in this work to describe H_2O - H_3BO_3 interactions. The iterative procedure described in Section 2.4 was performed for a single H_3BO_3 molecule in a box containing 100 H_2O molecules. The H_2O positions were equilibrated using NVT Monte Carlo at 300 K and then held fixed to reduce the number of DFT calculations required for force field fitting. Next, the cyclical procedure described in Section 2.4 was applied to fit H_2O - H_3BO_3 interactions. The results of this fitting are shown in the Supporting Information **Figure S15**.

2.6 Monte Carlo Simulations

All Monte Carlo simulations in this work were performed using RASPA.[91] In all simulations, the positions of framework (Si, Al, O) atoms were held fixed. This rigid framework approximation has been demonstrated to be appropriate for adsorption simulations in zeolites based on previous work by Daou et al.[93] and Vlugt and Schenk.[94] Electrostatic energies were calculated using the Ewald summation method. A 10 Å cutoff was used for vdW interactions; all unit cells were constructed to ensure that each lattice parameter was greater than 20 Å, satisfying the minimum image convention. Lennard-Jones potentials were truncated with a tail correction.

2.6.1 Widom Insertion

In contrast to most reported adsorption calculations, the calculations performed in this work model adsorption from aqueous solution rather than gas phase. Following the method of Xiong et al.[95], we calculated the adsorption of boric acid from aqueous solution by calculating the fugacity of a dilute solute using the following equation (1):

$$f_A = \rho k_B T (e^{(\frac{\mu_A^{\infty}}{k_B T})}) x_A \quad (1)$$

where f_A is the fugacity of component A, ρ is the number density of the solvent, k_B is Boltzmann's constant, T is the temperature, μ_A^{∞} is the excess chemical potential of the solute, and x_A is the mole fraction of the solute.

Widom insertion[96] calculations were used to calculate the excess chemical potential of boric acid in aqueous solution at infinite dilution (μ^{∞}_{H3BO3}). For these calculations, a cubic box with a side length of 24 Å was filled with 459 molecules of SPC/E water to match the density of SPC/E water predicted by NIST.[97] This was followed by 25000 cycles of NVT Monte Carlo at 300 K to generate an equilibrated configuration of H_2O molecules. To avoid convergence issues associated with low acceptance probabilities of insertion/deletion moves[95], a Continuous Fractional Component Monte Carlo (CFCMC) scheme was used. CFCMC was developed by Shi and Maginn[98] to overcome the challenges of insertion and deletion of molecules in dense systems.

The CFCMC-Widom Insertion calculations used 50000 equilibration cycles followed by 100000 production cycles. Thermodynamic properties were averaged over these production cycles. To ensure convergence, these calculations were repeated ten times with different random number seeds, and the final value was an average of these ten different calculations.

2.6.2 Parallel Tempering

The distribution of extra-framework cations has a strong effect on the adsorption properties of zeolites. Because of the presence of many deep local minima on the cation-framework potential energy surface, it is necessary to use a replica-exchange Monte Carlo technique called Parallel Tempering to equilibrate the positions of these cations.[81] These simulations were carried out using RASPA. Following the work of Fang et al.[57,88], nine structural replicas were used at T = 300 K, 390 K, 507 K, 659 K, 857 K, 1114 K, 1448 K, 1882 K, and 2447 K.[81]

2.6.3 Grand Canonical Monte Carlo

Grand Canonical Monte Carlo (GCMC) simulations were used to predict adsorption equilibrium for H_2O and H_3BO_3 in cationic zeolites using RASPA[91]. In these simulations, the positions of the framework atoms (Si, Al, O) were held fixed, while the extra-framework cations were allowed to move because the locations of extra-framework cations can have a significant effect on adsorption isotherms.[57,80,99,100]

Single-component water adsorption isotherms were computed in Na-FAU and Na-LTA to compare model predictions to experimental data. Adsorption isotherms were computed using GCMC in RASPA. The moves performed on water molecules were translation, rotation, reinsertion, insertion, and deletion with equal probability. Simulations were initialized with 10^4 Monte Carlo cycles followed by 10^4 production cycles. Loadings were computed using block averages. The component loading confidence intervals were observed to be < 10% of the simulated loading at most pressures. The zeolite framework coordinates (Si, Al, O) were taken from experimental data by Olson for Na-FAU[101], and Pluth and Smith for Na-LTA.[102] Both LTA and FAU zeolites have sodalite cages, which are inaccessible to adsorbates such as CO_2 and CH_4.[103,104] However, the relatively small H_2O molecules may be able to access these cages, so sodalite cages were not blocked in H_2O adsorption calculations. The SPC/E water model does not correctly predict the saturation pressure for water. Therefore, the horizontal axis was expressed as P divided by the saturation pressure, P_0, where P_0 for simulations was the SPC/E value (1.017 kPa) and the P_0 for the experimental measurements was the experimental value (3.533 kPa).[105]

For two-component mixed H_2O/H_3BO_3 simulations, the fugacity of H_3BO_3 was calculated using Equation (1) for each concentration studied. The saturation pressure of SPC/E water at 300 K computed by NIST[97] was used as the fugacity of H_2O in the simulations. Mole fractions of each component in solution were selected to correspond to 1 ppm, 5 ppm, 10 ppm, 15 ppm, and 20 ppm levels of H_3BO_3, which are typical levels for impoundment sites.[2] The large number of water molecules in zeolite pores results in a low acceptance probability of insertion/deletion moves using a conventional growth scheme. Therefore, it was necessary to apply CFCMC to obtain a

statistically robust sample. CFCMC-GCMC simulations were initialized over 10000 cycles followed by 5000 equilibration cycles over which the CFCMC weights for individual lambda values were determined. Thermodynamic properties were then averaged over 90000 production cycles. Properties were determined by block averaging using 5 blocks and error bars were based on a 95% confidence interval. These simulation parameters typically gave error bars < 15% of loadings. Better convergence could be obtained by increasing the number of production cycles, but it would have significantly slowed the screening process due to the large number of adsorbates present.

3. Results and Discussion

3.1 Force Field Validation

3.1.1 Cation - Framework Interactions

Comparisons between cation positions determined via experimental data and force field-based parallel tempering simulations were used for validation of the cation-framework force field. Predictions of adsorption isotherms, particularly those of quadrupolar molecules such as CO_2, are known to be sensitive to the equilibrium positions and motion of extra-framework cations.[80,88,100] Therefore, it is important to have an accurate model for cation-framework interaction energies when predicting adsorption of polar molecules such as H_2O[69,106] and H_3BO_3.

The distribution of extra-framework cations in Zeolite A has been well-studied for many different cationic species.[89,102,107,108] **Figure 2** illustrates the three main types of cation positions in the LTA zeolite; 4-membered ring sites are shown in green, 6-membered ring sites are shown in yellow, and 8-membered ring sites are shown in blue. Using parallel tempering simulations, the distribution of cations was predicted in four LTA zeolites with various cations. **Table 1** shows a comparison between experimental and simulated cation distributions for Na-LTA (Zeolite 4A)[102], Na/Ca-LTA (Zeolite 5A)[107], Ca-LTA[89], and Mn/Na-LTA[108]. In these four zeolites, calcium and manganese show a strong preference for the 6-membered rings where they can be stabilized by 6 nearby framework O-atoms, each carrying a partial negative charge. They are rarely observed in 8-membered ring sites, likely because of the larger ring size. Sodium can be found in either 8-membered rings, 6-membered rings, or 4-membered rings in Na-LTA (Zeolite 4A)[102], but is typically found only in 6-membered rings in LTA zeolites containing Ca and Mn.[89,108] Our predictions for the distribution of Na/Ca-LTA, Ca-LTA, and Na/Mn-LTA match the experimentally-observed distribution perfectly, and our predictions for the distribution of Na-LTA are in good agreement with the experimentally-observed distribution. The number of cations located in the 6-membered rings in Na-LTA was predicted perfectly and the majority of remaining cations were also located consistent with experimental results. A minor discrepancy for Na-LTA is that in the simulation, there are 31 total Na+ in 8-membered rings, while experiments show 24. This difference can be attributed to a few cations located in 8-membered rings instead of adjacent

4-membered rings. No 6-membered rings were doubly occupied. A similar result was previously reported in a study in which the same force field for Na-zeolite interactions was employed.[88] Additional validation for CHA and FAU zeolites is shown in **Tables S2** and **S3** of the Supporting Information.

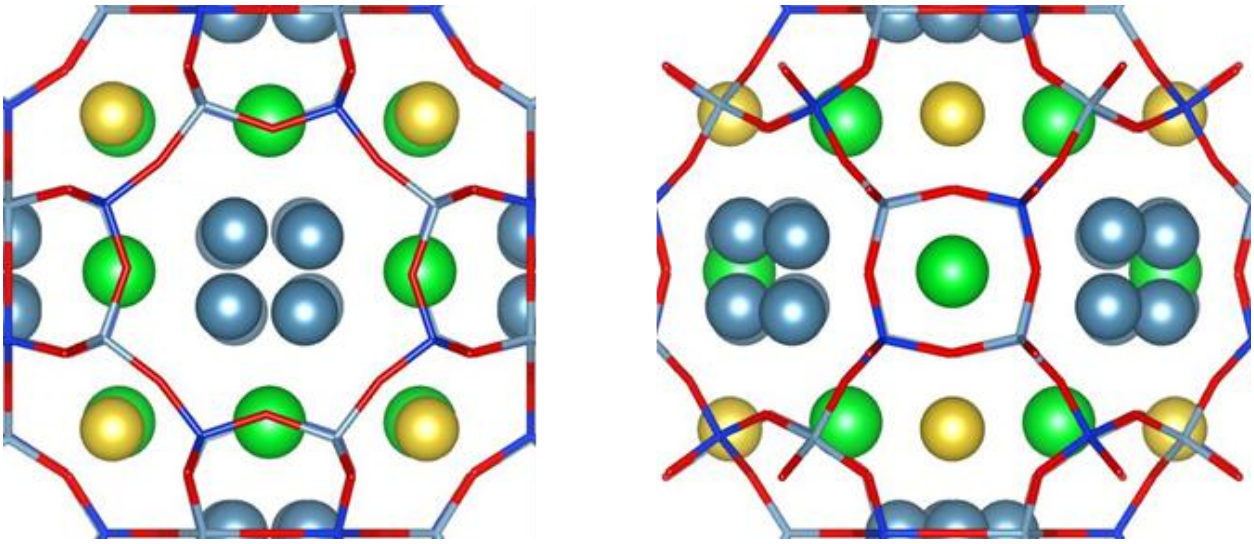

Figure 2: The crystallographic sites for cation locations in the LTA zeolite are shown. Cations are typically found in either 8-membered ring sites (blue), 6-membered ring sites (yellow) or 4-membered ring sites (green).

Zeolite	Cation	Number in 6-MR	Number in 8-MR	Number in 4-MR
Na-LTA	Na	64 (64)	31 (24)	1 (8)
Ca-LTA	Ca	48 (48)	0 (0)	0 (0)
Na/Ca-LTA	Ca	32 (32)	0 (0)	0 (0)
Na/Ca-LTA	Na	32 (32)	0 (0)	0 (0)
Mn/Na-LTA	Mn	36 (36)	0 (0)	0 (0)
Mn/Na-LTA	Na	24 (24)	0 (0)	0 (0)

Table 1: shows a comparison between experimental and simulated cation distributions for Na-LTA[88,102], Ca-LTA[89], Zeolite 5A[107], and Mn/Na-LTA[108]. The numbers in the table indicate the number of cations in each distinct type of site per simulation cell. The experimental values are shown in parentheses.

3.1.2 H_3BO_3 - Zeolite Interactions

An important limitation of classical 'non-reactive' force field models is that they typically cannot handle bond-breaking or bond-formation phenomena. To apply a classical non-reactive force field to this problem, we must ensure that the probability of bonds being formed or broken during the adsorption process is low. DFT optimizations were used to examine the likelihood for H_3BO_3 proton dissociation to one of the zeolite framework oxygens. The calculations show that there is no energy barrier for a dissociated proton from H_3BO_3 to hop back to the parent molecule. For these calculations, Na-exchanged LTA (Si/Al = 3) was examined with a loading of 10 H_2O molecules and 1 H_3BO_3 molecule. Next, AIMD trajectories were used to investigate the likelihood of proton hopping at finite temperature. All AIMD runs started with dissociated H_3BO_3 molecules and the protons quickly hopped back to the undissociated state. The details of these calculations are presented in the supporting information in section S6.

3.1.3 H_2O - Zeolite Interactions

Parameters for H_2O - cation interactions were fit using the procedure described in Section 2.4, and the accuracy of the force field was evaluated via a comparison of simulations to experimentally-measured water vapor adsorption isotherms. To ensure transferability between high Si/Al and low Si/Al zeolites, the O (zeolite) - O (H_2O) interaction parameters were taken from a first-principles force field by Findley et al.[109] This force field was able to predict correctly water intrusion in pure-silica MFI. Adsorbate-cation interactions for Na and Ca were described using a Buckingham + Coulomb potential. When examining the minimum adsorbate-cation distance vs. vdW contribution, it was observed that all values were positive, requiring the use of a fully-repulsive Buckingham potential (C=0) to get an accurate fit to PBE+D2 interaction energies. **Figure S14** in the **Supporting Information** shows the values of r_{min} vs. E_{vdw} in a training set for Na - H_2O interactions. Fe and Mn both had a mix of positive and negative vdW contributions. Therefore, Mn - H_2O and Fe - H_2O interactions were modeled using a Lennard-Jones + Coulomb potential. All parameters are shown in **Table S4**.

Force fields fit for H_2O were compared to experimental data in two well-studied zeolites, NaY (FAU topology) and 4A (LTA topology). Starting from sets of experimental framework coordinates, Na positions were predicted using Parallel Tempering. Next, GCMC simulations were used to predict water vapor adsorption isotherms, computed without blocking sodalite cages. Comparison with experimental data and predictions made by two existing (experimentally-derived) force fields[69,106] are shown for LTA (**Figure 3a**) and FAU (**Figure 3b**). The experimental data for the LTA zeolite shown in **Figure 3a** exhibits a large spread in the interval $0.001 < P/P_0 < 0.8$, but the experiments are mostly reproducible for pressures outside of this region. The differences between the experimentally measured isotherms in this region may be caused by structural differences in the samples, such as defects. When comparing the new D2FF predictions with experimental data, agreement was best at low loading and near saturation. The pressures corresponding to these regions are shown in green and blue respectively. The low-pressure ($P/P_0 < 0.001$) simulations are accurate because the DFT calculations used while fitting this model

contained 1 H_2O per unit cell. Therefore, D2FF energies would be the closest to DFT energies at low loadings of H_2O. At high pressures ($P/P_0 \approx 1$), the H_2O-H_2O interactions dominate, and the SPC/E water model has been shown to accurately predict the density of liquid water.[97] At intermediate pressures ($0.001 < P/P_0 < 0.8$) there is poor agreement which could be attributed to the water-zeolite energies being fit to DFT, while the water-water interaction energies were described based on the SPC/E model. It was noted by Castillo et al.[69] that polarizable force fields may be necessary to accurately predict adsorption in this regime. For the purpose of this work, accurate performance for the high-pressure region is the most important because fugacities in the saturation region are comparable to that of liquid water. Accurate predictions of adsorption at low pressures demonstrate accuracy of H_2O interaction energies with the cationic adsorption sites. Additionally, the D2FF predictions without blocked sodalite cages agree well with experimental data near saturation pressure of H_2O. This indicates that these small cages are likely accessible to H_2O, which has also been suggested in the literature.[69,110] For the H_2O vapor adsorption isotherms in Na-LTA, the D2FF performed better than the experimentally-derived force field of Fuchs et al.[106] but worse than the force field from Castillo et al.[69] This is a result of the force field of Castillo et al.[69] being fit to reproduce experimental isotherms in Na-LTA. The positions were reversed for simulations in Na-FAU (NaY), where Fuchs et al.[106] fit a force field to that set of experimental data. Overall, the D2FF was more transferable than either of the experimentally-derived force fields, indicating that the D2FF could be suitable for screening applications.

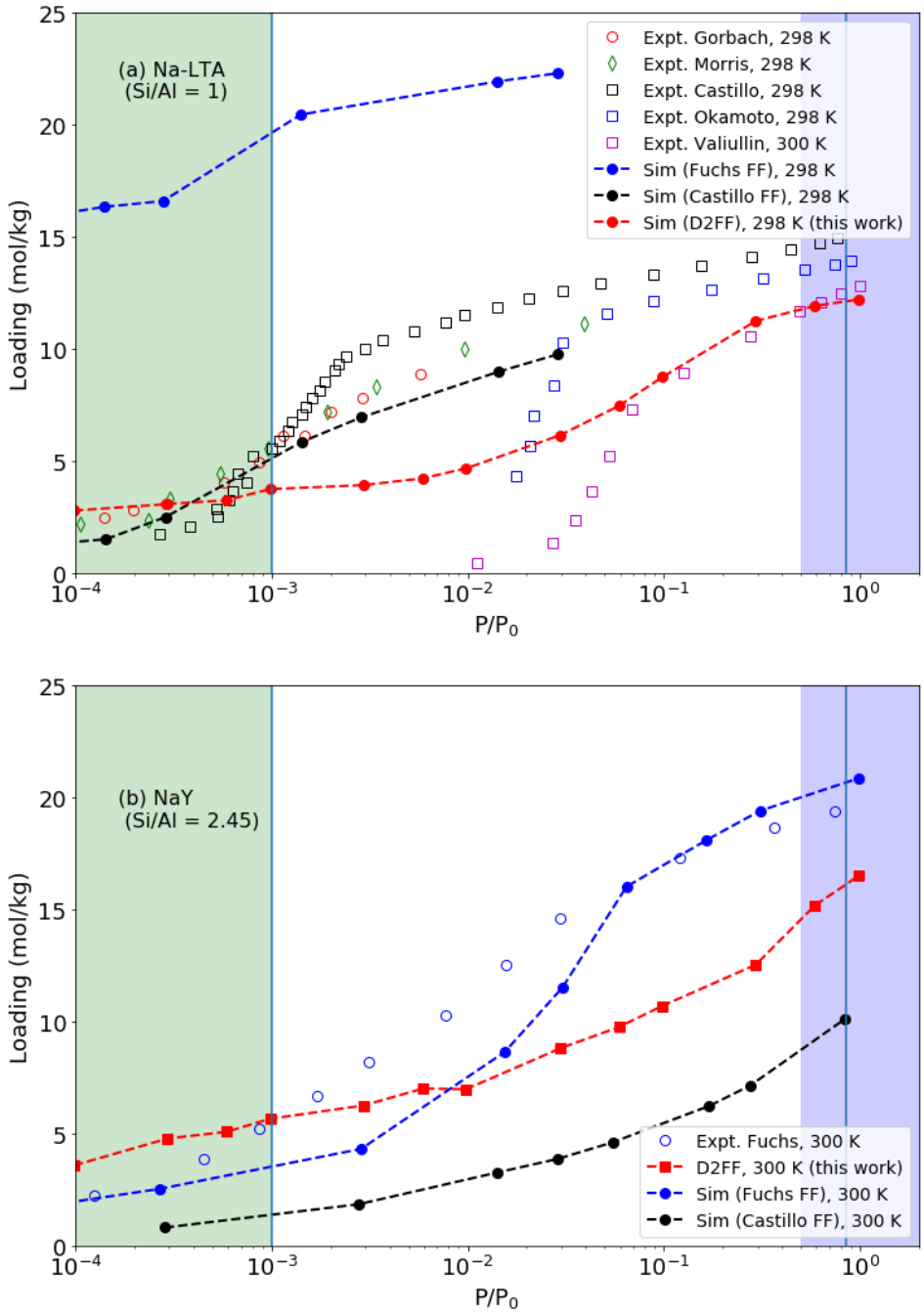

Figure 3: Shows a comparison between experimental (open symbols) and simulated (filled symbols) water loading in Na-LTA (Si/Al = 1) (a) and NaY (Si/Al = 2.45) (b). The D2FF force field fit in this work (red) was benchmarked against two force fields[69,106] that were parameterized based on experimental data (blue, black). The D2FF was more transferable across zeolite topology than either experimental force field.

3.1.4 H_3BO_3-H_2O Interactions

Calculations involving the adsorption of boric acid from solution require an accurate description of the chemical potential of the reference state. To validate the description of dilute boric acid in water, Widom Insertion simulations were performed using the CFCMC method.[98] From these calculations, it is possible to determine the excess chemical potential of infinitely-dilute boric acid, as well as the Henry's Law constant for boric acid in water. The computed Henry's Law constant of $1.29*10^{-7}$ Pa*m^3/mol was in agreement with the reported value from the Hazardous Substances Data Bank, which is $2.65*10^{-7}$ Pa*m^3/mol.

3.2 Predictions of H_3BO_3 Adsorption from Aqueous Solution

It is important to assess the transferability of the force field parameters for different zeolite compositions and topologies. It is important to verify the force field performance for zeolites with lower Si/Al ratios because any error in pairwise adsorbate-cation interactions will be more noticeable. To validate the transferability of force field parameters, the performance of parameters was tested in zeolite Ca-LTA (Si/Al = 3), Na/Ca-LTA (Si/Al = 1.7), and Mn-LTA (Si/Al = 3) by comparing DFT-predicted adsorption energies with force field-predicted adsorption energies. These energies were also benchmarked against energies computed using a combination of UFF Lennard-Jones terms and DDEC3 point charges. The results of these comparisons are shown in **Figure 4**.

For Si/Al = 3 LTA, a single LTA cage was used for faster DFT calculations. However, to distribute Al in a manner that satisfies Löwenstein's rule for LTA (Si/Al = 1.7), a 1x1x2 supercell was necessary. All cation positions were initialized using parallel tempering and then optimized using DFT. In the case of Na/Ca-LTA, an equal number of Na and Ca ions were present. Next, boric acid configurations were determined using a NVT Monte Carlo simulation. To reduce the number of required DFT calculations, extra-framework cation positions were held fixed during the NVT Monte Carlo simulation. Adsorption energies were calculated by subtracting the energy of the empty zeolite and isolated adsorbate from the energy of the zeolite with boric acid.

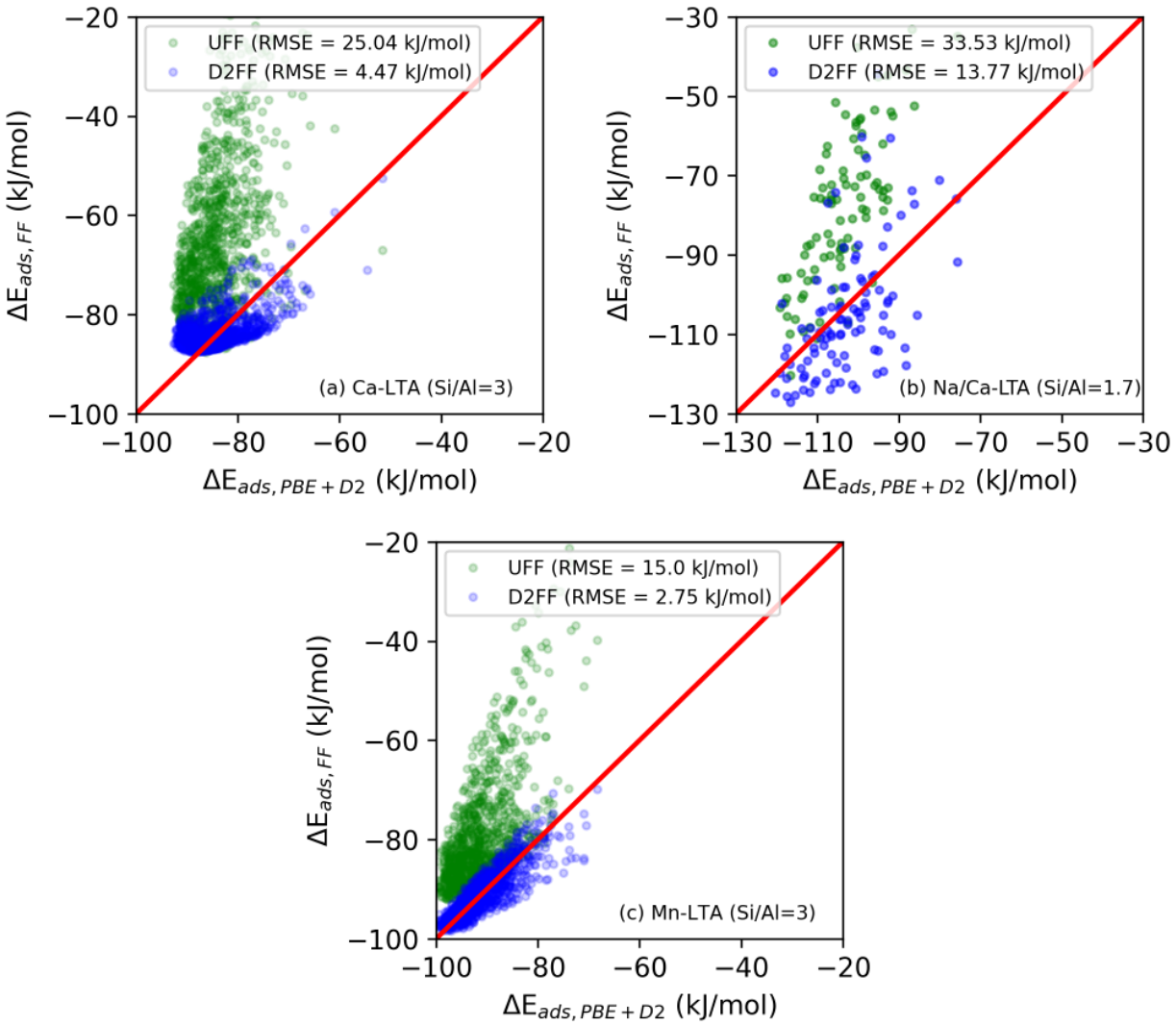

Figure 4: Comparisons between D2FF in blue (this work) and UFF in green and DFT adsorption energies for boric acid are shown for LTA to assess force field transferability to H_3BO_3 adsorption in zeolites with various cation identities, Si/Al ratios, and a different topology, LTA. The force field for H_3BO_3 was fit using DFT data calculated on CHA, Si/Al = 3.5. The results are shown for Ca-LTA (Si/Al = 3) (a), Na/Ca-LTA (Si/Al = 1.7) (b), and Mn-LTA (Si/Al = 3). The root mean square errors (RMSEs) for both force fields are shown at the top of each figure and indicate that the D2FF shows roughly half the error compared to the UFF force field.

The strongest interaction energies for the Si/Al=1.7 zeolite (b) were nearly 30 kJ/mol stronger than that of the Si/Al = 3 zeolite, which highlights a difficult challenge for the force field with regard to transferability as well as the importance of multi-cation adsorption sites. A similar type of adsorption has been observed for CO_2 in cationic zeolites[80,111], where both oxygens in CO_2 can interact with a distinct cation, resulting in "dual cation" sites. Following this nomenclature, it is possible for boric acid to adsorb on single, dual, and triple cation sites. It should also be noted that the interaction energies for both LTA zeolites are significantly lower than those of the CHA

zeolites used for training. The cation positions in the original force field training were selected in a manner that allowed for shorter boric acid-cation distances due to the positions of 8-membered ring cations. However, in both cases, LTA cations are "shielded" by negatively charged oxygen atoms, resulting in weaker electrostatic interactions between boric acid and the zeolite. The interaction for these "multi-cation" adsorption sites is dominated by electrostatics. The good agreement between energies calculated using D2FF and DFT for the most negative configurations indicates the accuracy and transferability of the DDEC3 point charges used in this model.

Our goal is to screen the entire material space of zeolites. Due to the computational expense of DFT calculations, the force field presented here was trained on a selected zeolite topology and Si/Al ratio. DFT calculations are computationally tractable only for zeolite frameworks that can be modeled with a small unit cell containing relatively few atoms. Despite this limitation, the force field energies for the most favorable H_3BO_3 configurations for zeolite topologies and Si/Al ratios outside the training set were typically within 10% of the energies calculated using DFT. This level of accuracy holds even when mixed cation zeolites were evaluated in the case of **Figure 4(b)**. These errors are not unexpected in the application of an interatomic potential to a wide and diverse material space and an error on this order of magnitude was considered reasonable for a screening study. Additionally, the RMSEs for the D2FF force field (between 2 and 14 kJ/mol) compare favorably against the UFF force field, (RMSE between 15 and 34 kJ/mol), which has been widely used for screening in porous materials, such as MOFs and zeolites, demonstrating that the D2FF is sufficiently accurate for screening purposes. Identification of promising zeolites from the large material space using a screening-quality force field could be followed by more detailed studies using a topology-specific custom-made force field or machine learned force field.

3.3 Screening of Zeolites

Adsorption simulations were performed for a set of Na-, Ca-, Mn-, and Fe-exchanged zeolites, as well as 3:1, 1:1, and 1:3 binary mixtures of each distinct cation pair. Cation positions were predicted using Parallel Tempering as in Fang et al.[57] Next, adsorption simulations were performed for 1 ppm, 5 ppm, 10 ppm, 15 ppm, and 20 ppm concentrations of boric acid. Because of the hydrophilic nature of cationic zeolites, multicomponent GCMC was used to account for adsorption of both boric acid and water. Fugacities of boric acid in the liquid phase were calculated in a similar manner to the method of Xiong et al.[95] However, in this work the excess chemical potential of dilute boric acid was calculated using the CFCMC Widom Insertion method rather than the Expanded Ensemble method.

3.3.1 Single Cation

The boric acid uptake of zeolites containing a single cation species (Na, Ca, Mn, or Fe) is shown in **Figure 5,** which shows the associations between boric acid loading and the mole fraction of aluminum on zeolite tetrahedral sites. In **Figure 5(a)**, data points are color-coded based on topology, while in **Figure 5(b)**, they are color-coded based on cation species. Both figures

demonstrate that as the fraction of T-sites occupied by Al (low Si/Al ratio) increases towards 0.5, the maximum boric acid uptake increases. The x_{Al} value of 0.5 corresponds to Si/Al = 1, which is the maximum Al content allowed by Lowenstein's Rule. The top-performing zeolite topologies were CHA, PHI, and LTA. A visualization of these three topologies is shown in **Figure S19** of the Supporting Information. All of these zeolites have been previously synthesized from fly ash.[15] **Figure 5(b)** shows that zeolites containing Ca (blue) performed best. This is likely caused by the high charge density on the Ca^{2+} cation, which leads to strong electrostatic interactions with boric acid molecules. **Figure 5(c)** shows that both the identity (charge) and the number of cations influence boric acid uptake. Including more cations per unit volume increases boric acid uptake for a given cation species because the cations act as boric acid adsorption sites. However, monovalent cations balance out the charge for one Al atom, while divalent cations (Ca, Mn(II), and Fe(II)) balance out the presence of two Al atoms. Therefore, a zeolite with a given Si/Al ratio can contain twice as many monovalent cations as it can divalent cations. This increase in possible adsorption sites led to higher performance for Na-exchanged zeolites over some of their Mn and Fe-exchanged counterparts as shown in **Figure 5(b) and (c)**. This tradeoff between cation number and cation charge indicates that it may be useful to study the performance of mixed-cation zeolites. Mn-and Fe-exchanged zeolites were predicted to have the lowest uptake for two possible reasons. First, the point charges on Mn (+1.28) and Fe (+1.09) were closer to Na (+0.99) than to Ca (+1.72), resulting in significantly weaker adsorbate-adsorbent interactions than Ca but with fewer sites than Na-exchanged zeolites. Additionally, Mn (72 pm), Fe (69 pm) are the smallest cations included in the study. They have been shown through experiments and in this work to preferentially occupy 6-membered ring sites. However, their small size allows them to locate closer to the plane of the 6-membered rings, causing the framework oxygen atoms to "shield" these cations more from adsorbates. This is consistent with the XRD experiments of Yanagida et al.[108]

While there are strong associations between composition and boric acid uptake, **Figure 5(d)** shows that there is no strong correlation between boric acid uptake and the ratio of largest cavity diameter (LCD) to pore-limiting diameter (PLD) in this set of zeolites. There was also no correlation observed with any other common geometric descriptors such as PLD, LCD, accessible volume, or accessible surface area. The boric acid uptake does depend on topology, as shown in **Figure 5(a)**. However, it is likely that scalar descriptors, such as PLD and LCD, do not contain enough topological information to produce strong correlations with boric acid uptake.

The optimal single-cation zeolite for boric acid uptake from 10 ppm solution is Ca-PHI(Si/Al = 1), according to **Figure 5**, which has a boric acid uptake of approximately 1.31 mol/kg. This corresponds to approximately 80.8 mg/g, which is approximately 5 times larger than the experimental results of Ulatowska et al. (16.14 mg/g) for fly ash.[14] This indicates that optimization of zeolite topology and composition can significantly improve zeolite performance for boron removal from water.

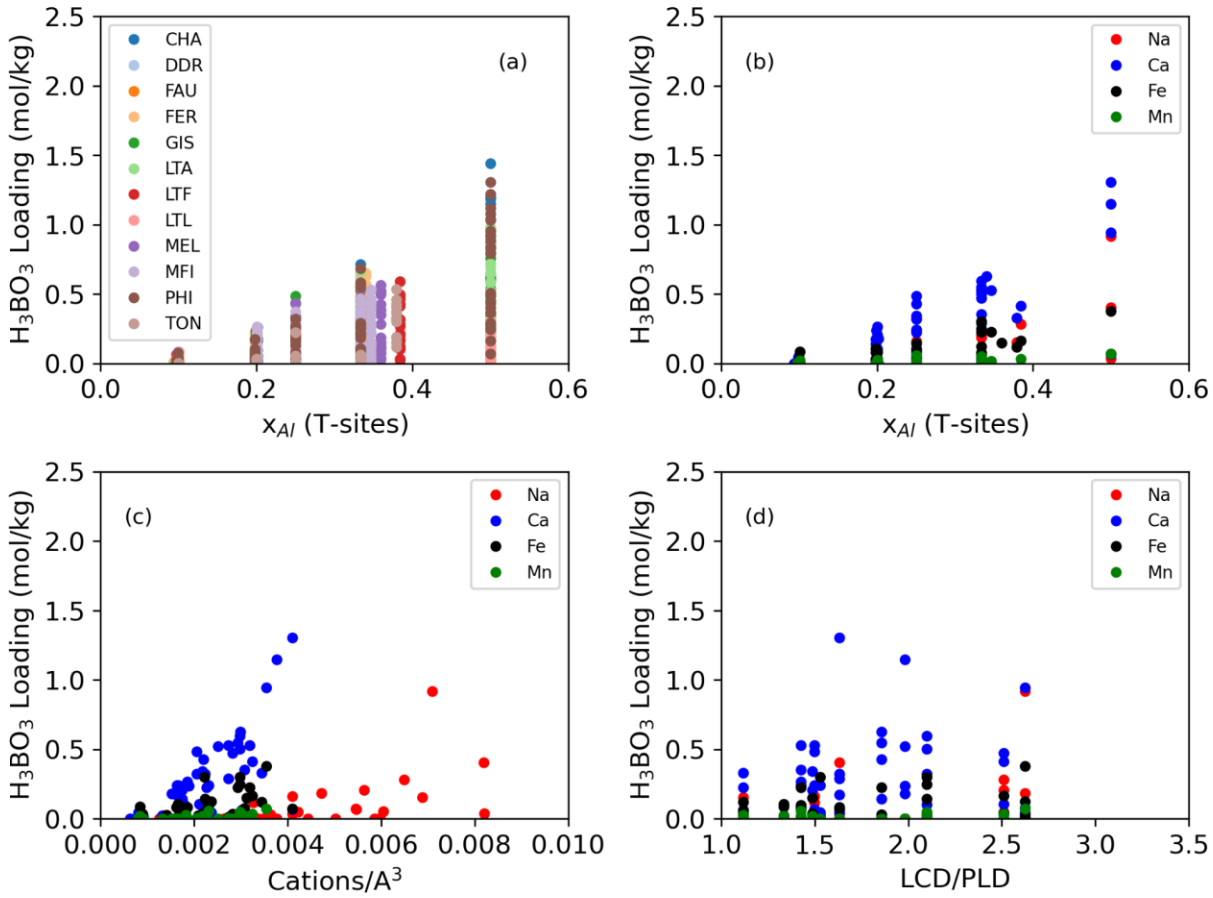

Figure 5: A detailed relationship between cation composition and boric acid uptake from 10 ppm boric acid solution is shown, which is the lowest concentration included in this study. The loadings as a function of aluminum content are shown color-coded by IZA topology (a) and cation identity (b). The dependence of boric acid uptake on the number of cations per volume is shown in (c) and the dependence on the ratio of LCD to PLD was shown in (d).

3.3.2 Mixed-Cation

The tradeoff between cation number and cation charge shown in **Figure 5(c)** indicates that both the charge of the cation and the number of cations per unit volume play a role in boric acid uptake. Therefore, adsorption simulations for all possible pairs of Na, Ca, Mn, and Fe were performed. The ratio of each species varied from 1:3, 1:1 and 3:1. The results for mixed cation zeolites are shown in **Figure 6** for zeolites containing Na(a), Ca(b), Mn(c), and Fe(d).

In the case of Na, Ca, and Mn, it is found that mixing cations can enhance performance over the original zeolite. For Na, adding Ca greatly improves performance because the point charge assigned to Ca using the DDEC method is significantly larger than the charges assigned to the other three cations. This results in stronger electrostatic interactions. In the case of Mn and Ca, adding Na improves boric acid uptake by adding more cations than would be present in the zeolite containing only Mn or Ca. This allows boric acid molecules to interact with more cations at once.

Mixing Fe with an amount of Ca improved performance, but it never exceeded the uptake of the pure Ca-exchanged zeolite. This is likely caused by the low partial charge on Fe compared to the other two divalent cations. After introducing mixed cations, the new optimal zeolite is Na/Ca-CHA with Si/Al = 1 and a Na:Ca ratio of 1:2. The predicted uptake is 1.44 mol/kg, which is almost 0.3 mol/kg higher than pure Ca-CHA with Si/Al = 1.

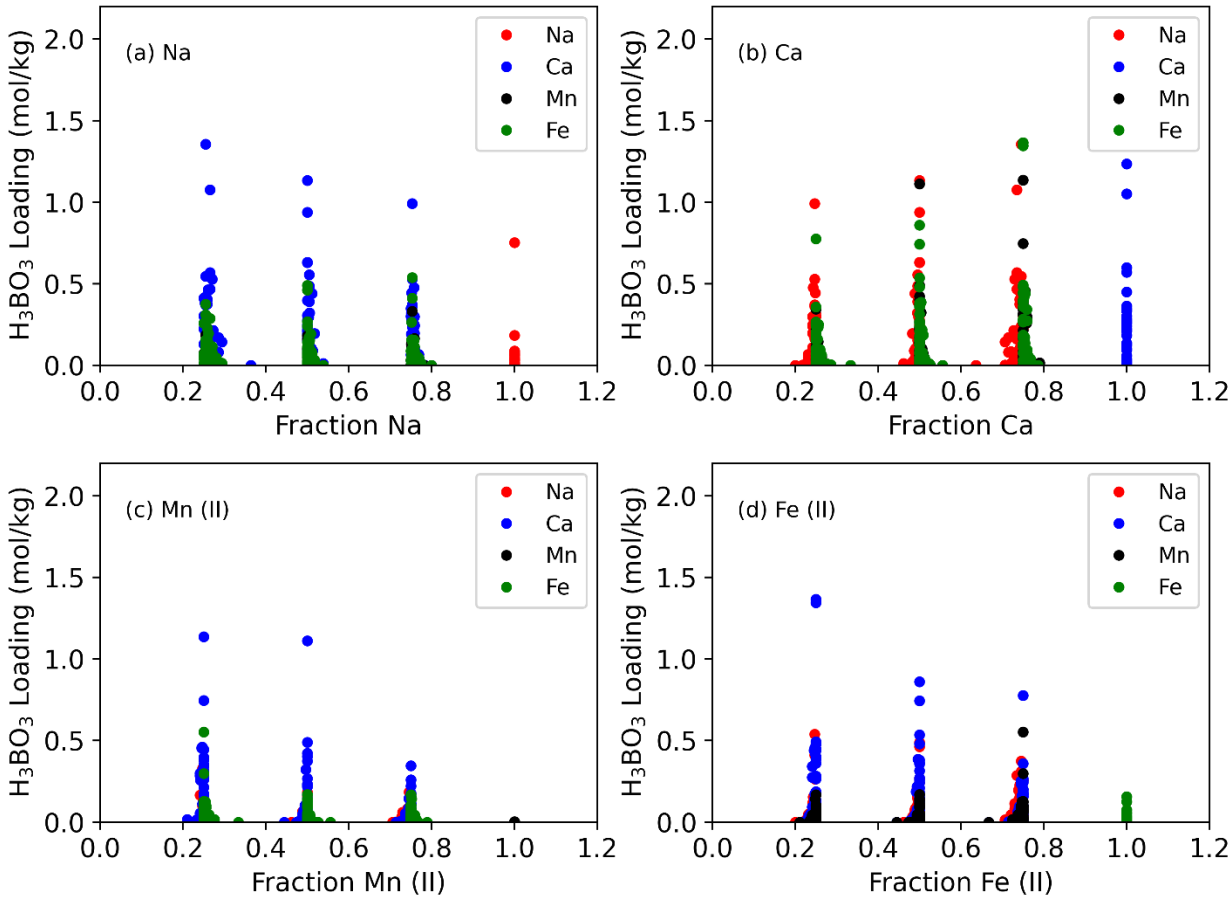

Figure 6 Shows a comparison between mixed cation zeolites and single-cation zeolites. The graphs are color coded based on the secondary cation. Na is shown in red, Ca in blue, Mn(II) in black, and Fe(II) in green.

3.3.3 Concentration Dependence

Figure 7 shows the boric acid uptake dependence on concentration in CHA, PHI, FAU, and LTA zeolites with Si/Al = 1 that are exchanged with Na, Ca, or a mixture of the two. The concentration range of 1 - 20 ppm was selected as representative of actual impoundment sites[2]. Most zeolites, especially Ca-exchanged zeolites, exhibited very little concentration dependence on boric acid uptake in this regime. The results from the GCMC simulations indicate that for Ca-exchanged zeolites, all or nearly all Ca atoms are within 3 angstroms of a boric acid molecule. Therefore, cationic sites are effectively saturated by boric acid. The non-monotonic dependence

on concentration is likely caused by the stochastic error involved with simulating a multicomponent system with one component near saturation.

This is not the case for some Na-exchanged zeolites, especially in Na-PHI and Na/Ca-CHA (75% Na), where there is a noticeable uptake increase with concentration over the 1 - 20 ppm range. This is likely because the smaller charge on Na leads to less selectivity for boric acid over water on the individual adsorption sites. Therefore, increasing the boric acid concentration has a larger effect on the boric acid uptake. This indicates that Na-exchanged zeolites may be optimal at high concentrations of boric acid.

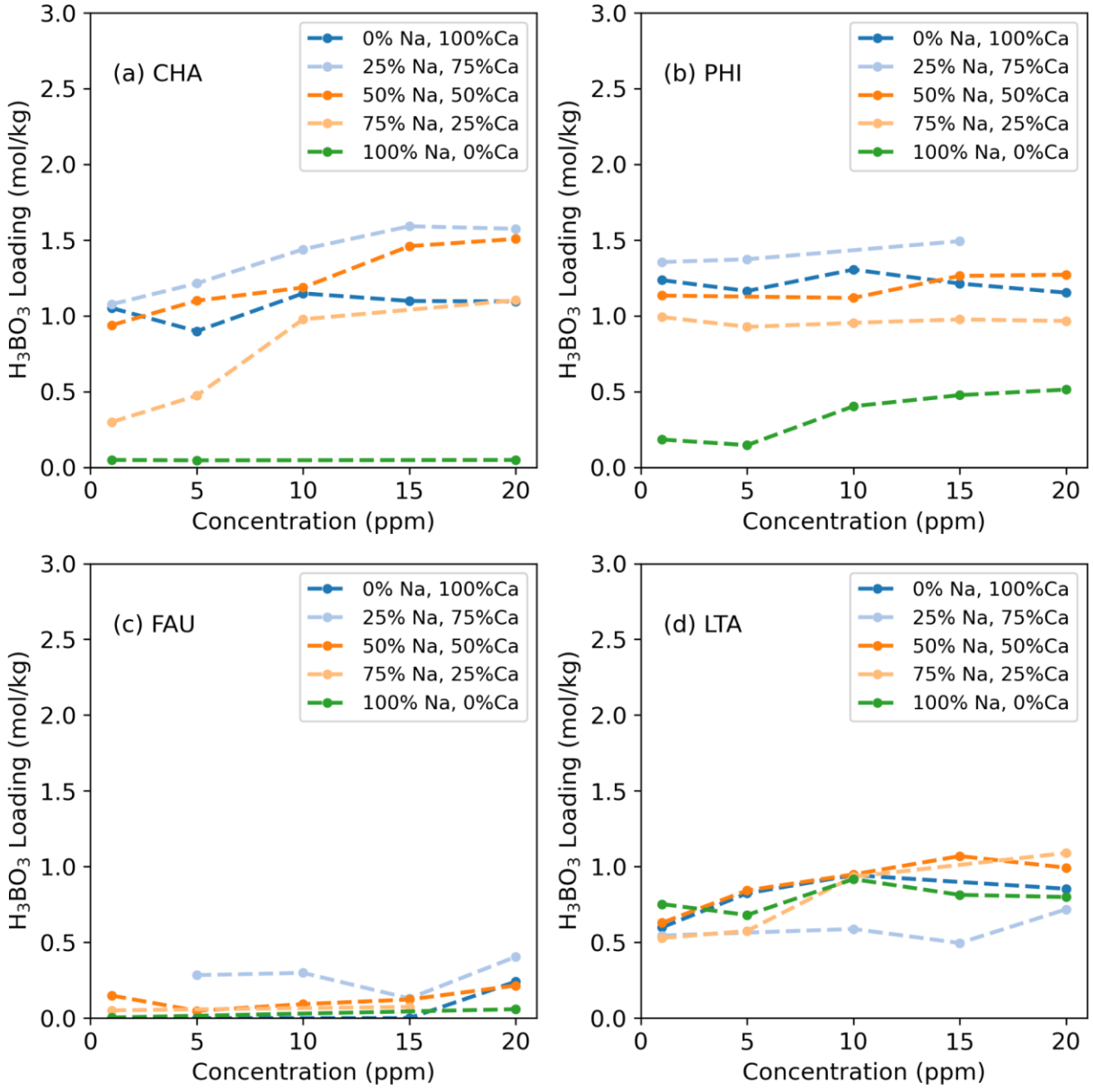

Figure 7: Dependence of boric acid uptake on boric acid concentration for CHA(a), PHI(b), FAU(c), and LTA(d). All zeolites in this figure had Si/Al = 1 and mixtures of Na/Ca. The

combinations of cations were shown for 100% Na (green), 75%Na, 25%Ca (peach), 50%Ca, 50%Na (orange), 25%Na, 75%Ca (light blue), and 100%Ca (dark blue).

Zeolites CHA, PHI, and LTA all had significantly higher uptakes than FAU regardless of composition in **Figure 7**. Based on these results, there was little to no selectivity for boric acid over water in FAU. To examine this effect, the cation-cation radial distribution functions (RDFs) were computed and shown in **Figure 8** for the same four zeolites.

Figure 8 shows the cation-cation radial distribution functions for CHA, PHI, FAU, and LTA. Peaks appear in the 6-8Å range for each of these zeolites except for FAU, which also showed the lowest boric acid uptake. This 6-8 Å spacing is characteristic of dual-cation sites, which promote CO_2 adsorption[53,80,111]. The O-O intramolecular distance for the H_3BO_3 molecule (2.36 Å) is comparable to that of the CO_2 molecule (2.32Å), suggesting that this spacing of cations may also enhance the adsorption of boric acid. To confirm the existence of dual cation adsorption and validate the force fields used, DFT calculations were used to determine the optimal adsorption configuration and energy for H_3BO_3 in three LTA zeolites with Si/Al = 1 (100% Na, 1:1 Na:Ca, and 100% Ca-exchanged). The results are shown in **Figure S16** and **Table S5** of the Supporting Information. All three zeolites showed multi-cation adsorption configurations, with Na-LTA adsorbing H_3BO_3 in a triple cation site, while Na/Ca-LTA and Ca-LTA adsorbed H_3BO_3 with a dual cation site. All cation-cation distances in the adsorption complex were between 6Å and 8Å, which is consistent with the force-field-based RDF peaks. The DFT energies of the three optimized adsorption configurations are all larger than 200 kJ/mol, which is roughly twice as large as the interaction energies computed by DFT for the force field training shown in **Figures S10-S13**. Based on these observations, multi-cation adsorption sites are predicted based on both force field-based RDFs shown in **Figure 8** as well as by DFT calculations described in **Figure S16** and give zeolite selectivity for boric acid over water. This is consistent with the strong relationship between Si/Al ratio and boric acid uptake shown previously in **Figures 5a and 5b**. Additionally, the presence of mixed monovalent/divalent cations gives more opportunities for the higher charge cations to interact in the form of multi-cation sites, causing improved performance for mixed-cation zeolites.

Based on experiments[112,113] and the simulations performed for **Table 1**, 6-membered windows are the optimal locations for Ca^{2+} cations. In the FAU topology, these sites are located between the sodalite cages and the supercage and between the hexagonal prism units and the sodalite cages. The sodalite-supercage sites are spaced too far apart in the pores to form dual-cation sites, while the hexagonal prism units and sodalite cages are inaccessible to boric acid molecules. The PHI topology also does not have 6-membered rings, so all Ca^{2+} was observed in the 8-membered ring sites during our simulations. Cations in the 8-membered rings in PHI are located between 6Å and 7Å from each other, which is an ideal distance for multi-cation adsorption, resulting in high uptake in PHI zeolites. CHA also has effectively fewer possible 6-membered ring sites for Ca^{2+} than LTA caused by the presence of hexagonal prism building units. The increased

accessibility of 8-membered ring cations, caused by less shielding by the zeolite framework, also resulted in a high uptake in CHA at low Si/Al ratios.

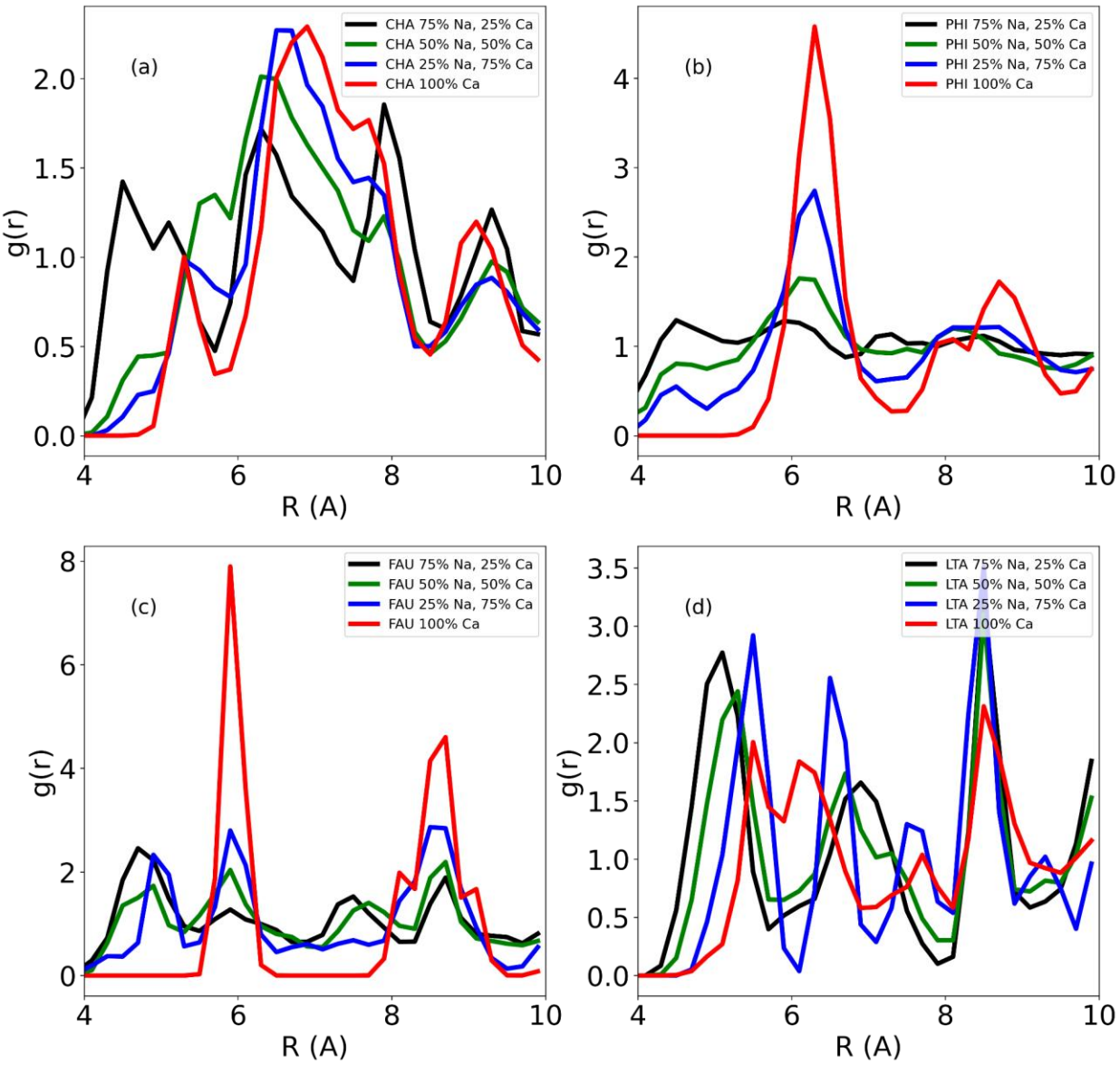

Figure 8: The cation-cation RDFs are shown for Na- and Ca-exchanged CHA (a), PHI (b), FAU (c), and LTA (d) with Si/Al = 1 for a range of 4 Å - 10 Å.

4. Data Availability and Reproducibility Statement

4.1 Data available in the Supplementary Materials

Several types of data were produced in this work. Density functional theory data was produced in this work according to methods described in the methods section of the manuscript

and further details are presented in the Supporting Information file. Density functional theory output files (OUTCAR files) are provided in the supplementary material zip file (SI_FF_BoricAcid.zip). (Figure 1) Also produced in this work are force field parameters; the force field definition files as used in the RASPA code are provided as part of the supplementary material zip file (SI_FF_BoricAcid.zip). Also provided are the RASPA input files for the continuous fractional component Monte Carlo simulations and all zeolite structural files for zeolites (including point charges) included in the study (SI_FF_BoricAcid.zip). Water adsorption isotherms, boric acid adsorption energies, calculated boric acid sorption, and cation-cation radial distribution functions are tabulated and provided as part of the supplementary material (SI_FF_BoricAcid.zip). (Figure 3-8).

4.2 Steps Taken to Ensure Reliability and Reproducibility

To ensure reproducibility of simulations, input files for RASPA simulations and output files for DFT calculations were provided. When determining final force field parameters using the iterative approach described in Section 2, Lennard-Jones parameters were considered converged when they varied by < 10% between training cycles. To ensure converged results for Monte Carlo simulations, adsorption properties were computed using block averages with 5 blocks. Error bars, which corresponded to 95% confidence intervals, were typically < 15% of the loading.

5. Conclusions

In conclusion, D2FF force fields were fit to predict cation distributions, boric acid adsorption, and water adsorption in aluminosilicate zeolites containing Na, Ca, Mn, and Fe. To assess the transferability of the D2FF models, they were compared to PBE+D2 energies for boric acid adsorption in zeolites of a different topology and composition from the original force field training data. This comparison was benchmarked against the performance of the generic UFF model. RMSEs for the D2FF were between 2 and 14 kJ/mol while those for the UFF force field were between 15 and 34 kJ/mol), showing that the new D2FF force fields represent a large improvement in accuracy compared to previously available methods. The improved accuracy and transferability of the D2FF model demonstrates that it is suitable for screening purposes. These force fields were used to predict the equilibrium adsorption uptakes of boric acid and water for a concentration range that is typical of impoundment ponds.

The boric acid uptake was shown to be controlled primarily by cation number, which is determined by the Si/Al ratio, the cation oxidation state, and the cation point charge. Higher numbers of cations (lower Si/Al) resulted in significantly higher boric acid adsorption, and higher cation charges (Ca) also enhanced adsorption due to strong electrostatic interactions. The tradeoff between higher cation charge versus more cations of lower charge was examined by simulating mixed-cation zeolites. It was observed that partially exchanging zeolites with a mixture of +1 and +2 cations, such as Na/Ca, resulted in improved adsorption of boric acid. The DFT-optimized

structures for H_3BO_3 in Na, Ca and Na:Ca-LTA illuminate a multi-cation adsorption motif in which the OH groups of the H_3BO_3 interact with several extra-framework cations simultaneously. The multi-cation adsorption motifs are consistent with the force field based radial distribution function results which exhibited peaks in the 6-8Å range known to be associated with multi-site adsorption. The presence of Ca^{2+} in 8-membered rings in PHI and low Si/Al CHA gave those two topologies the highest uptake of H_3BO_3.

Based on this dataset of approximately 6000 points, it should be possible to train a machine learning model to tailor sorbents to individual impoundment sites based on crystal structure and composition-based descriptors. This would allow for more efficient composition optimization as well as predictions for a larger set of zeolite topologies, many of which have not yet been synthesized from fly ash. Future work can also involve targeted predictions for individual high-performing zeolites, such as Na/Ca-PHI and Na/Ca-CHA, based on DFT methods or machine-learned force fields. These methods could also be applied to fitting interactions of the zeolites with other contaminants such as arsenic, selenium and mercury.

Author Contributions

J.F Conceptualization, methodology, software, visualization, and writing.
E.J.G. Conceptualization, project administration, writing.
E.G. Project administration, writing.
J.S. Conceptualization, methodology, project administration, writing and supervision.

Conflicts of Interest

There are no conflicts to declare.

Supplementary Material

- Supporting Information for Zeolite Sorption of Boric Acid from Aqueous Solution Using First Principles Force Fields (DOC)
- Also supplied are RASPA input files and structures used for simulations, OUTCAR files for DFT calculations for training a H_3BO_3 force field in CaCHA and computed boric acid uptake for all zeolites (SI_FF_BoricAcid.zip)

Acknowledgements

The authors gratefully acknowledge Dan Sorescu for helpful discussions and comments and Jeffrey Summers and the Emissions Control Program of the U.S. DOE for support of the research. This project was funded by the U.S. Department of Energy, National Energy Technology

Laboratory, in part, through a site support contract. Neither the United States Government nor any agency thereof, nor any of their employees, nor the support contractor, nor any of their employees, makes any warranty, express or implied, or assumes any legal liability or responsibility for the accuracy, completeness, or usefulness of any information, apparatus, product, or process disclosed, or represents that its use would not infringe privately owned rights. Reference herein to any specific commercial product, process, or service by trade name, trademark, manufacturer, or otherwise does not necessarily constitute or imply its endorsement, recommendation, or favoring by the United States Government or any agency thereof. The views and opinions of authors expressed herein do not necessarily state or reflect those of the United States Government or any agency thereof.

Literature Cited

1. Xu Y, Jiang JQ. Technologies for Boron Removal. *Ind Eng Chem Res*. 2008;47(1):16-24. doi:10.1021/ie0708982

2. EPRI. *Review of Coal Combustion Product Leaching: Summarizing EPRI Research, 1980-2021*.; 2021.

3. EPRI. *Chemical Constituents in Coal Combustion Products: Boron*.; 2020.

4. EPRI, Southern Company, AEP, South Carolina Electric and Gas Corporate Planning. *Chemical Constituents in Coal Combustion Product Leachate: Arsenic*.; 2008.

5. Chen L, Stehouwer R, Tong X, Kost D, Bigham JM, Dick WA. Surface coal mine land reclamation using a dry flue gas desulfurization product: Short-term and long-term water responses. *Chemosphere*. 2015;134:459-465. doi:10.1016/j.chemosphere.2015.05.014

6. Organization WH, WHO. *Guidelines for Drinking-Water Quality*. Vol 1. World Health Organization; 2004.

7. Waggott A. An investigation of the potential problem of increasing boron concentrations in rivers and water courses. *Water Res*. 1969;3(10):749-765. doi:https://doi.org/10.1016/0043-1354(69)90039-6

8. Kluczka J, Ciba J, Trojanowska J, Zolotajkin M, Turek M, Dydo P. Removal of boron dissolved in water. *Environ Prog*. 2007;26(1):71-77. doi:10.1002/ep.10180

9. Hilal N, Kim GJ, Somerfield C. Boron removal from saline water: A comprehensive review. *Desalination*. 2011;273(1):23-35. doi:10.1016/j.desal.2010.05.012

10. Demetriou A, Pashalidis I. Adsorption of boron on iron-oxide in aqueous solutions. *Desalination Water Treat*. Published online 2012:7. doi:https://doi.org/10.1080/19443994.2012.661288

11. Edzwald JK, Haarhoff J. Seawater pretreatment for reverse osmosis: Chemistry, contaminants, and coagulation. *Water Res*. 2011;45(17):5428-5440. doi:10.1016/j.watres.2011.08.014

12. Rajaković LV, Ristić MD. Sorption of boric acid and borax by activated carbon impregnated with various compounds. *Carbon*. 1996;34(6):769-774. doi:https://doi.org/10.1016/0008-6223(96)00009-7

13. Yüksel S, Yürüm Y. Removal of Boron from Aqueous Solutions by Adsorption Using Fly Ash, Zeolite, and Demineralized Lignite. *Sep Sci Technol*. 2009;45(1):105-115. doi:10.1080/01496390903256042

14. Ulatowska J, Polowczyk I, Bastrzyk A, Koźlecki T, Sawiński W. Fly ash as a sorbent for boron removal from aqueous solutions: Equilibrium and thermodynamic studies. *Sep Sci Technol*. 2020;55(12):2149-2157. doi:10.1080/01496395.2019.1612434

15. Querol X, Moreno N, Umaña JC, et al. Synthesis of zeolites from coal fly ash: an overview. *Int J Coal Geol*. 2002;50(1-4):413-423. doi:10.1016/S0166-5162(02)00124-6

16. Guozhi L, Zhang T, Cheng C, et al. Zeolite a preparation from high alumina fly ash of china using alkali fusion and hydrothermal synthesis method. *Mater Res Express*. 2019;6(6):065049. doi:10.1088/2053-1591/aafd4c

17. Murayama N, Yamamoto H, Shibata J. Mechanism of zeolite synthesis from coal fly ash by alkali hydrothermal reaction. *Int J Miner Process*. 2002;64(1):1-17. doi:10.1016/S0301-7516(01)00046-1

18. Liu H. Conversion of Harmful Fly Ash Residue to Zeolites: Innovative Processes Focusing on Maximum Activation, Extraction, and Utilization of Aluminosilicate. *ACS Omega*. 2022;7(23):20347-20356. doi:10.1021/acsomega.2c02388

19. Kazemian H, Naghdali Z, Ghaffari Kashani T, Farhadi F. Conversion of high silicon fly ash to Na-P1 zeolite: Alkaline fusion followed by hydrothermal crystallization. *Adv Powder Technol*. 2010;21(3):279-283. doi:10.1016/j.apt.2009.12.005

20. Cardoso AM, Paprocki A, Ferret LS, Azevedo CMN, Pires M. Synthesis of zeolite Na-P1 under mild conditions using Brazilian coal fly ash and its application in wastewater treatment. *Fuel*. 2015;139:59-67. doi:10.1016/j.fuel.2014.08.016

21. Srinivasan A, Grutzeck MW. The Adsorption of SO_2 by Zeolites Synthesized from Fly Ash. *Environ Sci Technol*. 1999;33(9):1464-1469. doi:10.1021/es9802091

22. Zhu T, Zhang X, Han Y, Liu T, Wang B, Zhang Z. Preparation of Zeolite X by the Aluminum Residue From Coal Fly Ash for the Adsorption of Volatile Organic Compounds. *Front Chem*. 2019;7:341. doi:10.3389/fchem.2019.00341

23. Belviso C. State-of-the-art applications of fly ash from coal and biomass: A focus on zeolite synthesis processes and issues. *Prog Energy Combust Sci*. 2018;65:109-135. doi:10.1016/j.pecs.2017.10.004

24. Ojumu TV, Du Plessis PW, Petrik LF. Synthesis of zeolite A from coal fly ash using ultrasonic treatment – A replacement for fusion step. *Ultrason Sonochem*. 2016;31:342-349. doi:10.1016/j.ultsonch.2016.01.016

25. Baerlocher C, McCusker LB, Olson DH. *Atlas of Zeolite Framework Types*. Elsevier; 2007.

26. Deem MW, Pophale R, Cheeseman PA, Earl DJ. Computational discovery of new zeolite-like materials. *J Phys Chem C*. 2009;113(51):21353-21360. doi:https://doi.org/10.1021/jp906984z

27. Earl DJ, Deem MW. Toward a Database of Hypothetical Zeolite Structures. *Ind Eng Chem Res*. 2006;45(16):5449-5454. doi:10.1021/ie0510728

28. Lozinska MM, Mowat JP, Wright PA, et al. Cation gating and relocation during the highly selective "trapdoor" adsorption of CO2 on univalent cation forms of zeolite rho. *Chem Mater*. 2014;26(6):2052-2061. doi:https://doi.org/10.1021/cm404028f

29. Shang J, Li G, Singh R, et al. Discriminative separation of gases by a "molecular trapdoor" mechanism in chabazite zeolites. *J Am Chem Soc*. 2012;134(46):19246-19253. doi:https://doi.org/10.1021/ja309274y

30. Jale SR, Bülow M, Fitch FR, Perelman N, Shen D. Monte Carlo simulation of sorption equilibria for nitrogen and oxygen on LiLSX zeolite. *J Phys Chem B*. 2000;104(22):5272-5280. doi:https://doi.org/10.1021/jp993777r

31. Palomino M, Corma A, Rey F, Valencia S. New Insights on CO2- Methane separation using LTA zeolites with different Si/Al ratios and a first comparison with MOFs. *Langmuir*. 2010;26(3):1910-1917. doi:https://doi.org/10.1021/la9026656

32. Jíša K, Nováková J, Schwarze M, Vondrová A, Sklenák S, Sobalik Z. Role of the Fe-zeolite structure and iron state in the N2O decomposition: Comparison of Fe-FER, Fe-BEA, and Fe-MFI catalysts. *J Catal*. 2009;262(1):27-34. doi:10.1016/j.jcat.2008.11.025

33. Hevia MAG, Pérez-Ramírez J. Optimal Hydrocarbon Selection for Catalytic N_2O Reduction over Iron-Containing ZSM-5 Zeolite. *Environ Sci Technol*. 2008;42(23):8896-8900. doi:10.1021/es801971w

34. Di Iorio JR, Nimlos CT, Gounder R. Introducing catalytic diversity into single-site chabazite zeolites of fixed composition via synthetic control of active site proximity. *Acs Catal*. 2017;7(10):6663-6674. doi:https://doi.org/10.1021/acscatal.7b01273

35. Dědeček J, Tabor E, Sklenak S. Tuning the aluminum distribution in zeolites to increase their performance in acid-catalyzed reactions. *ChemSusChem*. 2019;12(3):556-576. doi:https://doi.org/10.1002/cssc.201801959

36. Lobo RF, Zones SI, Davis ME. Structure-direction in zeolite synthesis. *J Incl Phenom Mol Recognit Chem*. 1995;21(1):47-78. doi:https://doi.org/10.1007/BF00709411

37. Schwalbe-Koda D, Gómez-Bombarelli R. Supramolecular Recognition in Crystalline Nanocavities through Monte Carlo and Voronoi Network Algorithms. *J Phys Chem C*. 2021;125(5):3009-3017. doi:10.1021/acs.jpcc.0c10108

38. Gies H, Marker B. The structure-controlling role of organic templates for the synthesis of porosils in the systems SiO2/template/H2O. *Zeolites*. 1992;12(1):42-49. doi:https://doi.org/10.1016/0144-2449(92)90008-D

39. Moliner M, Rey F, Corma A. Towards the rational design of efficient organic structure-directing agents for zeolite synthesis. *Angew Chem Int Ed*. 2013;52(52):13880-13889. doi:https://doi.org/10.1002/anie.201304713

40. Demirçivi P, Nasün-Saygili G. Removal of boron from waste waters using HDTMA-modified zeolites. *Desalination Water Treat*. 2010;23(1):110-117. doi:10.5004/dwt.2010.1957

41. Dionisiou NS, Matsi T, Misopolinos ND. Removal of Boron by Surfactant Modified Zeolitic Tuff from Northeastern Greece. *J Agric Sci*. 2013;5(12):p94. doi:10.5539/jas.v5n12p94

42. Flores Díaz AA, Velázquez Machuca MA, Medina Ramírez A, et al. Boron adsorption on modified zeolites: Effect of modifier and source of water. *Rev Int Contam Ambient*. 2023;39. doi:10.20937/rica.54473

43. Lyu J, Zhang N, Liu H, et al. Adsorptive removal of boron by zeolitic imidazolate framework: kinetics, isotherms, thermodynamics, mechanism and recycling. *Sep Purif Technol*. 2017;187:67-75. doi:10.1016/j.seppur.2017.05.059

44. Altare CR, Bowman RS, Katz LE, Kinney KA, Sullivan EJ. Regeneration and long-term stability of surfactant-modified zeolite for removal of volatile organic compounds from produced water. *Microporous Mesoporous Mater*. 2007;105(3):305-316. doi:10.1016/j.micromeso.2007.04.001

45. Burtch NC, Jasuja H, Walton KS. Water Stability and Adsorption in Metal–Organic Frameworks. *Chem Rev*. 2014;114(20):10575-10612. doi:10.1021/cr5002589

46. Pérez-Botella E, Valencia S, Rey F. Zeolites in Adsorption Processes: State of the Art and Future Prospects. *Chem Rev*. 2022;122(24):17647-17695. doi:10.1021/acs.chemrev.2c00140

47. Lafuente B, Downs RT, Yang H, Stone N. 1. The power of databases: The RRUFF project. In: Armbruster T, Danisi RM, eds. *Highlights in Mineralogical Crystallography*. De Gruyter (O); 2015:1-30. doi:10.1515/9783110417104-003

48. Kluczka J, Trojanowska J, Zołotajkin M. Utilization of fly ash zeolite for boron removal from aqueous solution. *Desalination Water Treat*. 2015;54(7):1839-1849. doi:10.1080/19443994.2014.892033

49. De Lima RCF, Oliveira DDS, Pergher SBC. Interzeolitic Transformation of Clinoptilolite into GIS and LTA Zeolite. *Minerals*. 2021;11(12):1313. doi:10.3390/min11121313

50. Shevade S, Ford RG. Use of synthetic zeolites for arsenate removal from pollutant water. *Water Res*. 2004;38(14-15):3197-3204. doi:10.1016/j.watres.2004.04.026

51. Li J, Gao M, Yan W, Yu J. Regulation of the Si/Al ratios and Al distributions of zeolites and their impact on properties. *Chem Sci*. 2023;14(8):1935-1959. doi:10.1039/D2SC06010H

52. Fang H, Awati R, Boulfelfel SE, Ravikovitch PI, Sholl DS. First-principles-derived force fields for CH4 adsorption and diffusion in siliceous zeolites. *J Phys Chem C*. 2018;122(24):12880-12891. doi:https://doi.org/10.1021/acs.jpcc.8b03267

53. Nachtigall P, Delgado MR, Nachtigallova D, Areán CO. The nature of cationic adsorption sites in alkaline zeolites—single, dual and multiple cation sites. *Phys Chem Chem Phys*. 2012;14(5):1552-1569. doi:https://doi.org/10.1039/C2CP23237E

54. Fang H, Kamakoti P, Zang J, et al. Prediction of CO2 Adsorption Properties in Zeolites Using Force Fields Derived from Periodic Dispersion-Corrected DFT Calculations. *J Phys Chem C*. 2012;116(19):10692-10701. doi:10.1021/jp302433b

55. Shang J, Li G, Webley PA, Liu JZ. A density functional theory study for the adsorption of various gases on a caesium-exchanged trapdoor chabazite. *Comput Mater Sci*. 2016;122:307-313. doi:https://doi.org/10.1016/j.commatsci.2016.05.040

56. Fuchs AH, Cheetham AK. Adsorption of Guest Molecules in Zeolitic Materials: Computational Aspects. *J Phys Chem B*. 2001;105(31):7375-7383. doi:10.1021/jp010702q

57. Fang H, Kulkarni A, Kamakoti P, Awati R, Ravikovitch PI, Sholl DS. Identification of high-CO2-capacity cationic zeolites by accurate computational screening. *Chem Mater*. 2016;28(11):3887-3896. doi:https://doi.org/10.1021/acs.chemmater.6b01132

58. Sholl DS. Understanding macroscopic diffusion of adsorbed molecules in crystalline nanoporous materials via atomistic simulations. *Acc Chem Res*. 2006;39(6):403-411. doi:https://doi.org/10.1021/ar0402199

59. Gu C, Yu Z, Liu J, Sholl DS. Construction of an anion-pillared MOF database and the screening of MOFs suitable for Xe/Kr separation. *ACS Appl Mater Interfaces*. 2021;13(9):11039-11049. doi:https://doi.org/10.1021/acsami.1c00152

60. McDaniel JG, Li S, Tylianakis E, Snurr RQ, Schmidt J. Evaluation of force field performance for high-throughput screening of gas uptake in metal–organic frameworks. *J Phys Chem C*. 2015;119(6):3143-3152. doi:https://doi.org/10.1021/jp511674w

61. Keskin S, Sholl DS. Screening Metal- Organic framework materials for membrane-based methane/carbon dioxide separations. *J Phys Chem C*. 2007;111(38):14055-14059. doi:https://doi.org/10.1021/jp075290l

62. Kulkarni AR, Sholl DS. Screening of copper open metal site MOFs for olefin/paraffin separations using DFT-derived force fields. *J Phys Chem C*. 2016;120(40):23044-23054. doi:https://doi.org/10.1021/acs.jpcc.6b07493

63. Rappe AK, Casewit CJ, Colwell KS, Goddard WAI, Skiff WM. UFF, a full periodic table force field for molecular mechanics and molecular dynamics simulations. *J Am Chem Soc*. 1992;114(25):10024-10035. doi:10.1021/ja00051a040

64. Mayo SL, Olafson BD, Goddard WA. DREIDING: a generic force field for molecular simulations. *J Phys Chem*. 1990;94(26):8897-8909. doi:10.1021/j100389a010

65. Daglar H, Keskin S. Recent advances, opportunities, and challenges in high-throughput computational screening of MOFs for gas separations. *Coord Chem Rev*. 2020;422:213470. doi:10.1016/j.ccr.2020.213470

66. Kancharlapalli S, Snurr RQ. High-Throughput Screening of the CoRE-MOF-2019 Database for CO_2 Capture from Wet Flue Gas: A Multi-Scale Modeling Strategy. *ACS Appl Mater Interfaces*. 2023;15(23):28084-28092. doi:10.1021/acsami.3c04079

67. Findley JM, Sholl DS. Computational screening of MOFs and zeolites for direct air capture of carbon dioxide under humid conditions. *J Phys Chem C*. 2021;125(44):24630-24639. doi:https://doi.org/10.1021/acs.jpcc.1c06924

68. Bai P, Tsapatsis M, Siepmann JI. TraPPE-zeo: Transferable potentials for phase equilibria force field for all-silica zeolites. *J Phys Chem C*. 2013;117(46):24375-24387. doi:https://doi.org/10.1021/jp4074224

69. Castillo JM, Silvestre-Albero J, Rodriguez-Reinoso F, Vlugt TJ, Calero S. Water adsorption in hydrophilic zeolites: experiment and simulation. *Phys Chem Chem Phys*. 2013;15(40):17374-17382. doi:https://doi.org/10.1039/C3CP52910J

70. Fang H, Findley J, Muraro G, Ravikovitch PI, Sholl DS. A Strong Test of Atomically Detailed Models of Molecular Adsorption in Zeolites Using Multilaboratory Experimental Data for CO_2 Adsorption in Ammonium ZSM-5. *J Phys Chem Lett*. 2020;11(2):471-477. doi:10.1021/acs.jpclett.9b02986

71. Han SS, Choi SH, Goddard III WA. Zeolitic imidazolate frameworks as H2 adsorbents: Ab initio based grand canonical monte carlo simulation. *J Phys Chem C*. 2010;114(27):12039-12047. doi:https://doi.org/10.1021/jp103785u

72. Dzubak AL, Lin LC, Kim J, et al. Ab initio carbon capture in open-site metal–organic frameworks. *Nat Chem*. 2012;4(10):810-816. doi:https://doi.org/10.1038/nchem.1432

73. Lin LC, Lee K, Gagliardi L, Neaton JB, Smit B. Force-field development from electronic structure calculations with periodic boundary conditions: applications to gaseous adsorption and transport in metal–organic frameworks. *J Chem Theory Comput*. 2014;10(4):1477-1488. doi:https://doi.org/10.1021/ct500094w

74. Zang J, Nair S, Sholl DS. Prediction of water adsorption in copper-based metal–organic frameworks using force fields derived from dispersion-corrected DFT calculations. *J Phys Chem C*. 2013;117(15):7519-7525. doi:https://doi.org/10.1021/jp310497u

75. Fang H, Daou ASS, Boulfelfel SE, Findley JM, Ravikovitch PI, Sholl DS. Computational Screening of Cationic Zeolites for *n* -Butane/Methane Separations Using Quantitatively Accurate First-Principles-Derived Force Fields. *J Phys Chem C*. 2023;127(49):23941-23955. doi:10.1021/acs.jpcc.3c06115

76. Ociński D, Mazur P. Highly efficient arsenic sorbent based on residual from water deironing – Sorption mechanisms and column studies. *J Hazard Mater*. 2020;382:121062. doi:10.1016/j.jhazmat.2019.121062

77. Loewenstein W. The distribution of aluminum in the tetrahedra of silicates and aluminates. *Am Mineral J Earth Planet Mater*. 1954;39(1-2):92-96.

78. Dědeček J, Lucero MJ, Li C, et al. Complex analysis of the aluminum siting in the framework of silicon-rich zeolites. A case study on ferrierites. *J Phys Chem C*. 2011;115(22):11056-11064. doi:https://doi.org/10.1021/jp200310b

79. Di Iorio JR, Gounder R. Controlling the isolation and pairing of aluminum in chabazite zeolites using mixtures of organic and inorganic structure-directing agents. *Chem Mater*. 2016;28(7):2236-2247. doi:https://doi.org/10.1021/acs.chemmater.6b00181

80. Findley JM, Ravikovitch PI, Sholl DS. The Effect of Aluminum Short-Range Ordering on Carbon Dioxide Adsorption in Zeolites. *J Phys Chem C*. 2018;122(23):12332-12340. doi:10.1021/acs.jpcc.8b03475

81. Beauvais C, Guerrault X, Coudert FX, Boutin A, Fuchs AH. Distribution of Sodium Cations in Faujasite-Type Zeolite: A Canonical Parallel Tempering Simulation Study. *J Phys Chem B*. 2004;108(1):399-404. doi:10.1021/jp036085i

82. Kresse G, Hafner J. Ab initio molecular-dynamics simulation of the liquid-metal–amorphous-semiconductor transition in germanium. *Phys Rev B*. 1994;49(20):14251. doi:https://doi.org/10.1103/PhysRevB.49.14251

83. Kresse G, Furthmüller J. Efficient iterative schemes for ab initio total-energy calculations using a plane-wave basis set. *Phys Rev B*. 1996;54(16):11169. doi:https://doi.org/10.1103/PhysRevB.54.11169

84. Kresse G, Furthmüller J. Efficiency of ab-initio total energy calculations for metals and semiconductors using a plane-wave basis set. *Comput Mater Sci*. 1996;6(1):15-50. doi:https://doi.org/10.1016/0927-0256(96)00008-0

85. Grimme S. Semiempirical GGA-type density functional constructed with a long-range dispersion correction. *J Comput Chem*. 2006;27(15):1787-1799.

86. Watanabe T, Manz TA, Sholl DS. Accurate treatment of electrostatics during molecular adsorption in nanoporous crystals without assigning point charges to framework atoms. *J Phys Chem C*. 2011;115(11):4824-4836. doi:https://doi.org/10.1021/jp201075u

87. Manz TA, Sholl DS. Chemically meaningful atomic charges that reproduce the electrostatic potential in periodic and nonperiodic materials. *J Chem Theory Comput*. 2010;6(8):2455-2468. doi:https://doi.org/10.1021/ct100125x

88. Fang H, Kamakoti P, Ravikovitch PI, Aronson M, Paur C, Sholl DS. First principles derived, transferable force fields for CO 2 adsorption in Na-exchanged cationic zeolites. *Phys Chem Chem Phys*. 2013;15(31):12882-12894. doi:DOI https://doi.org/10.1039/C3CP52246F

89. Pluth JJ, Smith JV. Crystal structure of dehydrated calcium-exchanged zeolite A. Absence of near-zero-coordinate calcium (2+) ion. Presence of aluminum complex. *J Am Chem Soc*. 1983;105(5):1192-1195. doi:https://doi.org/10.1021/ja00343a019

90. Boulfelfel SE, Findley JM, Fang H, Daou AS, Ravikovitch PI, Sholl DS. A Transferable Force Field for Predicting Adsorption and Diffusion of Small Molecules in Alkali Metal Exchanged Zeolites with Coupled Cluster Accuracy. *J Phys Chem C*. 2021;125(48):26832-26846. doi:https://doi.org/10.1021/acs.jpcc.1c07790

91. Dubbeldam D, Calero S, Ellis DE, Snurr RQ. RASPA: molecular simulation software for adsorption and diffusion in flexible nanoporous materials. *Mol Simul*. 2016;42(2):81-101. doi:https://doi.org/10.1080/08927022.2015.1010082

92. Otkidach DS, Pletnev IV. Conformational analysis of boron-containing compounds using Gillespie–Kepert version of molecular mechanics. *J Mol Struct THEOCHEM*. 2001;536(1):65-72. doi:10.1016/S0166-1280(00)00602-3

93. Daou ASS, Findley JM, Fang H, Boulfelfel SE, Ravikovitch PI, Sholl DS. Quantifying Impact of Intrinsic Flexibility on Molecular Adsorption in Zeolites. *J Phys Chem C*. 2021;125(9):5296-5305. doi:10.1021/acs.jpcc.0c09952

94. Vlugt TJ, Schenk M. Influence of framework flexibility on the adsorption properties of hydrocarbons in the zeolite silicalite. *J Phys Chem B*. 2002;106(49):12757-12763. doi:https://doi.org/10.1021/jp0263931

95. Xiong R, Sandler SI, Vlachos DG. Alcohol Adsorption onto Silicalite from Aqueous Solution. *J Phys Chem C*. 2011;115(38):18659-18669. doi:10.1021/jp205312k

96. Widom B. Some topics in the theory of fluids. *J Chem Phys*. 1963;39(11):2808-2812.

97. Shen VK, Siderius D, Krekelberg W, Hatch H, others. NIST standard reference simulation website. *NIST Stand Ref Database*. 2017;173.

98. Shi W, Maginn EJ. Continuous Fractional Component Monte Carlo: An Adaptive Biasing Method for Open System Atomistic Simulations. *J Chem Theory Comput*. 2007;3(4):1451-1463. doi:10.1021/ct7000039

99. Pirngruber G, Raybaud P, Belmabkhout Y, Čejka J, Zukal A. The role of the extra-framework cations in the adsorption of CO 2 on faujasite Y. *Phys Chem Chem Phys*. 2010;12(41):13534-13546. doi:https://doi.org/10.1039/B927476

100. Yang X, Epiepang FE, Liu Y, Yang RT. Heats of adsorption on mixed-cation LiNa-LSX: estimating SIII site occupancy by Li. *Chem Eng Sci*. 2018;178:194-198. doi:https://doi.org/10.1016/j.ces.2017.12.039

101. Olson DH. The crystal structure of dehydrated NaX. *Zeolites*. 1995;15(5):439-443. doi:https://doi.org/10.1016/0144-2449(95)00029-6

102. Pluth JJ, Smith JV. Accurate redetermination of crystal structure of dehydrated zeolite A. Absence of near zero coordination of sodium. Refinement of silicon, aluminum-ordered superstructure. *J Am Chem Soc*. 1980;102(14):4704-4708. doi:https://doi.org/10.1021/ja00534a024

103. Keffer D, Gupta V, Kim D, Lenz E, Davis HT, McCormick AV. A compendium of potential energy maps of zeolites and molecular sieves. *J Mol Graph*. 1996;14(2):108-116. doi:https://doi.org/10.1016/0263-7855(96)00040-9

104. Bates SP, van Well WJ, van Santen RA, Smit B. Energetics of n-alkanes in zeolites: a configurational-bias Monte Carlo investigation into pore size dependence. *J Am Chem Soc*. 1996;118(28):6753-6759. doi:https://doi.org/10.1021/ja953856q

105. Bridgeman O, Aldrich E. Vapor pressure tables for water. Published online 1964.

106. Fuchs AH, Boutin A, Teuler JM, et al. Development and Application of Molecular Simulation Methods for the Screening of Industrial Zeolite Adsorbents. *Oil Gas Sci Technol - Rev IFP*. 2006;61(4):571-578. doi:10.2516/ogst:2006031a

107. Seff K, Shoemaker D. The structures of zeolite sorption complexes. I. The structures of dehydrated zeolite 5A and its iodine sorption complex. *Acta Crystallogr*. 1967;22(2):162-170. doi:https://doi.org/10.1107/S0365110X67000283

108. Yanagida RY, Vance TB, Seff K. Five-coordinate and three-coordinate manganese (II). Hydrated and dehydrated crystal structures of partially manganese (II)-exchanged zeolite A. *Inorg Chem*. 1974;13(3):723-727. doi:https://doi.org/10.1021/ic50133a042

109. Findley JM, Boulfelfel SE, Fang H, Muraro G, Ravikovitch PI, Sholl DS. A Transferable Force Field for Predicting Adsorption and Diffusion of Hydrocarbons and Small Molecules in Silica Zeolites with Coupled-Cluster Accuracy. *J Phys Chem C*. 2021;125(15):8418-8429. doi:https://doi.org/10.1021/acs.jpcc.1c00943

110. Beauvais C, Boutin A, Fuchs AH. Adsorption of water in zeolite sodium-faujasite: A molecular simulation study. *Comptes Rendus Chim*. 2005;8(3-4):485-490. doi:https://doi.org/10.1016/j.crci.2004.11.011

111. Pulido A, Nachtigall P, Zukal A, Domínguez I, Čejka J. Adsorption of CO2 on Sodium-Exchanged Ferrierites: The Bridged CO2 Complexes Formed between Two Extraframework Cations. *J Phys Chem C*. 2009;113(7):2928-2935. doi:10.1021/jp810038b

112. Pluth JJ, Smith JV. Crystal structure of dehydrated calcium-exchanged zeolite A. Absence of near-zero-coordinate calcium(2+) ion. Presence of aluminum complex. *J Am Chem Soc*. 1983;105(5):1192-1195. doi:10.1021/ja00343a019

113. Seff K, Shoemaker DP. The structures of zeolite sorption complexes. I. The structures of dehydrated zeolite 5 *A* and its iodine sorption complex. *Acta Crystallogr*. 1967;22(2):162-170. doi:10.1107/S0365110X67000283